

ALMA ^{12}CO (J=1–0) imaging of the nearby galaxy M83: Variations in the efficiency of star formation in giant molecular clouds

Akihiko Hirota,^{1,2} Fumi Egusa,^{1,3} Junichi Baba,^{4,1} Nario Kuno,^{5,6}
Kazuyuki Muraoka,⁷ Tomoka Tosaki,⁸ Rie Miura,¹ Hiroyuki Nakanishi,⁹
and Ryohei Kawabe^{1,10,11}

¹National Astronomical Observatory of Japan, 2-21-1 Osawa, Mitaka, Tokyo 181-8588, Japan

²Joint ALMA Observatory, Alonso de Córdova 3107, Vitacura, Santiago 763-0355, Chile

³Institute of Space and Astronautical Science, Japan Aerospace Exploration Agency,
Sagamihara, Kanagawa 252-5210, Japan

⁴Earth-Life Science Institute, Tokyo Institute of Technology, 2-12-1 Ookayama, Meguro, Tokyo
152-8551, Japan

⁵Division of Physics, Faculty of Pure and Applied Sciences, University of Tsukuba, 1-1-1
Tennodai, Tsukuba, Ibaraki 305-8571, Japan

⁶Tomonaga Center for the History of the Universe, University of Tsukuba, 1-1-1 Tennodai,
Tsukuba, Ibaraki 305-8571, Japan

⁷Department of Physical Science, Graduate School of Science, Osaka Prefecture University,
1-1 Gakuen-cho, Naka-ku, Sakai 599-8531, Japan

⁸Joetsu University of Education, Yamayashiki-machi, Joetsu, Niigata 943-8512, Japan

⁹Graduate School of Science and Engineering, Kagoshima University, 1-21-35 Korimoto,
Kagoshima, Kagoshima 890-0065, Japan

¹⁰SOKENDAI (The Graduate University for Advanced Studies), 2-21-1 Osawa, Mitaka, Tokyo
181-8588, Japan

¹¹Department of Astronomy, School of Science, University of Tokyo, Bunkyo, Tokyo 113-0033,
Japan

*E-mail: akihiko.hirota@nao.ac.jp

Received 2017 October 23; Accepted 2018 May 3

Abstract

We present results of the ^{12}CO (1–0) mosaic observations of the nearby barred-spiral galaxy M83 obtained with the Atacama Large Millimeter/submillimeter Array (ALMA). The total flux is recovered by combining the ALMA data with single-dish data obtained using the Nobeyama 45-m telescope. The combined map covers a ~ 13 kpc² field that includes the galactic center, eastern bar, and spiral arm with a resolution of $2''.03 \times 1''.15$ (~ 45 pc \times ~ 25 pc). With a resolution comparable to typical sizes of giant molecular clouds (GMCs), the CO distribution in the bar and arm is resolved into many clumpy peaks that form ridge-like structures. Remarkably, in the eastern arm, the CO peaks form two arc-shaped ridges that run along the arm and exhibit a distinct difference in the activity of star formation: the one on the leading side has numerous H II regions associated with it, whereas the other one on the trailing side has only a few. To see whether GMCs form stars with uniform star formation efficiency (SFE) per free-fall time (SFE_{ff}), GMCs are identified from the data cube and then cross-matched with the catalog of H II regions to estimate the star formation rate for each of them. 179 GMCs with a median mass of

$1.6 \times 10^6 M_{\odot}$ are identified. The mass-weighted average SFE_{ff} of the GMCs is $\sim 9.4 \times 10^{-3}$, which is in agreement with models of turbulence regulated star formation. Meanwhile, we find that SFE_{ff} is not universal within the mapped region. In particular, one of the arm ridges shows a high SFE_{ff} with a mass-weighted value of $\sim 2.7 \times 10^{-2}$, which is higher by more than a factor of 5 compared to the inter-arm regions. This large regional variation in SFE_{ff} favors the recent interpretation that GMCs do not form stars at a constant rate within their lifetime.

Key words: galaxies: individual (M83) — galaxies: ISM — galaxies: star formation — ISM: molecule

1 Introduction

As most star formation takes place in giant molecular clouds (GMCs) and as star formation is one of the fundamental processes that drives the evolution of galaxies, it is essential to understand the processes that determine the star formation efficiency (SFE) in GMCs.

Molecular clouds with sizes of 20–100 pc and masses of $10^{4-6} M_{\odot}$ are often classified as GMCs (e.g., Sanders et al. 1985; Solomon et al. 1987). Motions inside GMCs are turbulent with resultant CO linewidths of several kilometers per second, which are ‘supersonic’ for typical temperatures in GMCs (~ 10 K). Although early studies proposed that the turbulent linewidth could be a manifestation of the gravitational collapse of GMCs (e.g., Goldreich & Kwan 1974), in most places GMCs are assumed to be supported by turbulent pressure and magnetic fields against their self-gravity, and kept in near-virial equilibrium (e.g., Larson 1981; Solomon et al. 1987). The observed balance between the virial mass and the cloud mass derived with a reasonable assumption regarding the CO-to- H_2 conversion factor, also known as Larson’s second law, has been considered as one of the important manifestations of the nature of GMC that is close to the virial equilibrium.

In the Milky Way (MW), GMCs form stars with a low efficiency in the sense that only 1% of the GMC mass is converted into stars per free-fall time (Zuckerman & Evans 1974; Krumholz & McKee 2005). The low SFE was one of the earliest grounds for assuming that GMCs are in a state of near equilibrium rather than in a state of gravitational collapse because it was argued that if GMCs are in a state of collapse, more stars should be produced within a free-fall time. The recognition of the low efficiency led to another discussion on the idea that some mechanisms should be regulating the star formation rate (SFR) in GMCs.

In discussing mechanisms that regulate the SFE in GMCs, it is common practice to adopt a parameter called *star formation efficiency per free-fall time* (SFE_{ff}). The parameter is defined as $SFE_{\text{ff}} \equiv \tau_{\text{ff}} \text{SFR} / M_{\text{GMC}}$, where M_{GMC} and τ_{ff} are the mass and free-fall time of a cloud, respectively. As far as GMCs are concerned, the average value of SFE_{ff} is claimed to be uniform, approximately 0.01, in many galaxies, including the MW (Krumholz et al. 2012).

Turbulence is one of the mechanisms considered responsible for regulating SFE_{ff} . Turbulence could regulate star formation in a GMC by forming a small volume of high-density regions within it while keeping the bulk of the GMC in near virial balance (e.g., Mac Low & Klessen 2004). Attempts have been made to construct theoretical descriptions that quantitatively reproduce an SFE_{ff} of ~ 0.01 in a steady state (e.g., Krumholz & McKee 2005; Federrath 2015). The efforts trying to achieve $SFE_{\text{ff}} \sim 0.01$ in a steady state implies that GMCs are approximated as long-lived entities that form stars with constant efficiency.

However, although the model of turbulence regulated star formation succeeded in explaining the low average value of SFE_{ff} to a certain degree (Federrath 2015), some studies imply that the assumption of quasi-steady virialized GMCs could be oversimplifying the nature of GMCs. First, the lifetime of GMCs has been estimated to be 15–40 Myr, which is only a few τ_{ff} , by several studies; the GMC lifetime is suggested to be effectively limited by the disrupting roles of OB stars (Blitz & Shu 1980; Kawamura et al. 2009; Murray 2011; Miura et al. 2012) or large-scale shearing motions in inter-arm regions (Meidt et al. 2015). If this is true, then GMCs do not necessarily have to be long-lived entities that are kept in near virial balance. Second, Larson’s second law alone does not completely rule out the possibility that GMCs are collapsing because even if a GMC is in a state of free-fall, the CO linewidth increases by only a factor of $\sqrt{2}$ compared to a GMC in virial balance (Larson 1981). The difference is subtle and within the inevitable observational uncertainties. If GMCs are not long-lived as suggested by the first argument, they are allowed to be at least partially collapsing as was argued by Goldreich & Kwan (1974) (see Ballesteros-Paredes et al. 2011).

Further, recent studies point out that there is a wide spread, larger than two orders of magnitude, in SFE_{ff} observed for Galactic GMCs (Murray 2011; Lee et al. 2016; see also Mooney & Solomon 1988). Those authors argued that the large scatter in SFE_{ff} is hard explain by the models of turbulence-regulated star formation, which predict a weak dependence of SFE_{ff} on the properties of GMCs. Instead, they proposed that SFE_{ff} should be a time-dependent variable that dynamically increases during the lifetime of GMCs, although the effects of observational bias

must be carefully examined (Feldmann & Gnedin 2011).

Accepting that there is a wide scatter in SFE_{ff} , it is natural to think of its spatial distribution within a galaxy. If SFE_{ff} indeed increases dynamically during the lifetime of GMCs, there should be a variation in the observed SFE_{ff} across spiral arms because spiral arms have at least moderate impact in organizing the build-up and disruption of massive GMCs (Egusa et al. 2011; Hirota et al. 2011; Colombo et al. 2014). On the other hand, if SFE_{ff} is stable, then the distribution of SFE_{ff} observed should not exhibit strong spatial variations. Therefore, the investigation of the spatial distribution of SFE_{ff} in galaxies should provide a clue to understand how the rate of star formation is regulated in GMCs, a discussion that is closely connected with the nature of a GMC itself.

M83 is an ideal target to investigate SFE_{ff} in GMCs because it is one of the nearest (4.5 Mpc, Thim et al. 2003) spiral galaxies that is seen face-on and hosts prominent galactic structures, namely a bar and spiral arms. Metallicities in M83 are comparable to or even higher than in the MW (Bresolin et al. 2016), thus CO lines are effective in tracing molecular clouds. Other basic parameters of M83 are listed in table 1. As this galaxy contains a large amount of molecular gas ($3.2 \times 10^9 M_{\odot}$, Crosthwaite et al. 2002), numerous observational studies were made with both single-dish telescopes and interferometers (see references listed in Hirota et al. 2014). However, due to its low declination, interferometric observations made previous to the arrival of the Atacama Large Millimeter/submillimeter Array (ALMA) suffered from limited u - v samplings, and the spatial resolutions achieved were insufficient to resolve individual GMCs. Recently, Freeman et al. (2017) investigated the properties of GMCs in M83 using the ALMA data, but the data used lacked sensitivity to the total flux.

We present the results of ^{12}CO (1–0) mosaic observations of M83 taken with the ALMA. The interferometric data are combined with data taken with the Nobeyama 45-m telescope to recover the total flux. Target fields of the observations are selected so that a variety of galactic structures are covered, including the bar, the spiral arm, inter-arm regions, and the galactic center. We examine the observational properties of GMC including SFE_{ff} over galactic structures to see whether or not systematic variation in SFE_{ff} exists.

We describe the CO observations in section 2 and present the CO distribution in section 3. In section 4, we identify GMCs from the obtained CO data cube and examine their basic properties. Scaling relations of the properties of the identified GMCs and their mass functions are also examined. In section 5, by cross-matching the identified GMCs with H II regions, we derive SFE_{ff} for each GMC. In section 6, discussions are made to interpreting the meaning of the observed variation in SFE_{ff} and also to see in which regions feedback from massive stars is large enough to disrupt GMCs. In section 7, we present a summary.

Table 1. Adopted parameters of M83

Parameter	Value
Morph. ¹	SAB(s)c
Center position (J2000) ²	13 ^h 37 ^m 00 ^s .72 −29°51′57″.2
Position angle ³	225°
Inclination angle ³	24°
Systemic velocity (LSR) ⁴	514 km s ^{−1}
Distance ⁵	4.5 ± 0.3 Mpc
Linear scale	1″ ∼ 22 pc
SFR ⁶	3.0 M_{\odot} yr ^{−1}
HI mass ⁷	7.9 × 10 ⁹ M_{\odot}
H ₂ mass ⁸	3.2 × 10 ⁹ M_{\odot}
E(B-V) ⁹	0.070

¹ de Vaucouleurs et al. (1991). ² Thatte et al. (2000). ³ Comte (1981). ⁴ Kuno et al. (2007). ⁵ Thim et al. (2003). ⁶ Jarrett et al. (2013), adjusted to a distance of 4.5 Mpc. ⁷ Heald et al. (2016), adjusted to a distance of 4.5 Mpc. ⁸ Crosthwaite et al. (2002), adjusted to a distance of 4.5 Mpc. ⁹ Schlegel et al. (1998).

2 Observations and Data

2.1 ALMA observations

Aperture synthesis observations of the inner part of M83 in ^{12}CO (1–0) were carried out with the ALMA (program ID: 2011.0.00772.S). Observations were made with about 16 antennas that have 12m diameter each. The 64-input correlator was used to acquire cross-correlation data and configured to cover ∼1 GHz bandwidth around a center frequency of ∼114.92 GHz with a channel spacing of 0.244 MHz. As the Hanning window function was applied online, the effective frequency resolution was 0.488 MHz (∼1.27 km s^{−1}).

Figure 1(a) shows the target field of the ALMA observations. 45 pointings were observed sequentially with an integration time of ∼6 s per pointing, and J1316–336 was observed once in approximately 20 min as a time dependent gain calibrator. The absolute flux scale was calibrated using J1337–129 and Titan, and 3C279 was used for the passband calibration. The system noise temperature was in the range from 100 to 150 K throughout the observations.

The cross-correlated visibility data were processed with the standard ALMA calibration procedures using the CASA software package (McMullin et al. 2007; Petry & CASA Development Team 2012) to correct for atmospheric and instrumental phase fluctuations, and to transfer the temperature from the primary flux calibrators. These calibrations are made by applying calibration scripts bundled with the data set. Inspection of the antenna-based gain solutions and also the calibrated data showed that there was no need to further edit of the data. The calibrated visibility data were exported as UV-FITS and then converted to the MIRIAD (Sault et al. 1995) data format for the subsequent reduction process.

Before proceeding to the data combination, as a sanity check, the calibrated visibility data were Fourier-transformed

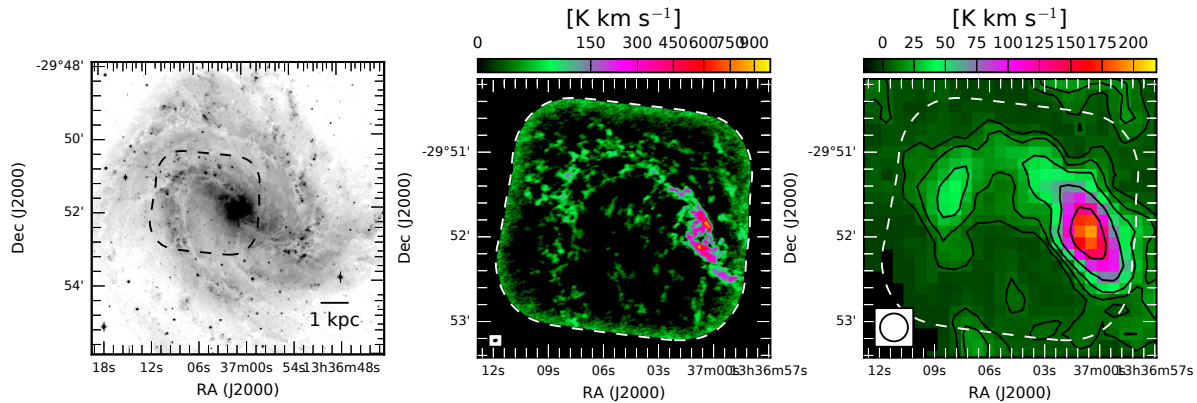


Fig. 1. (a) Optical V -band image of M83 taken from Larsen & Richtler (1999). (b) Velocity integrated intensity ^{12}CO (1–0) image of M83 generated from the ALMA data only. Due to the lack of sensitivity of zero-spacing data, extended emission are filtered out. (c) Same as (b), but for the data taken with 45-m telescope. The contour levels are 8, 16, 32, 64, and 128 K km s^{-1} . In each of these three plots, the dashed line indicates the field of view (FOV) of the ALMA mosaic observations with a normalized gain level of 0.9.

with natural weighting, and the CLEAN method was applied to produce the deconvolved image. The CLEAN beam was $2''.07 \times 1''.13$ with a position angle of $\sim -77^\circ.6$. The images were made for every two channels by averaging four neighboring channels to keep the resultant data cube oversampled in the velocity axis. Therefore, each channel in the resultant cube has a width of $\sim 1.27 \text{ km s}^{-1}$, but with an effective resolution of $\sim 2.54 \text{ km s}^{-1}$. After the deconvolution was performed, the spatial distribution of the rms noise was estimated from line free channels for each line of sight. Within the mapped area, the median value of the rms was $\sim 7.4 \text{ mJy}$ per beam with a velocity resolution of $\sim 2.54 \text{ km s}^{-1}$. However, we note that as the pointed mosaic observations made by the ALMA observing script assigned longer integration times to the southern half of the map, the spatial distribution of the noise is not uniform. The 16th and 84th percentiles of the rms noise were 6.1 and 10.3 mJy per beam, respectively. Figure 1(b) shows the integrated intensity map of the ALMA image in ^{12}CO (1–0).

2.2 45-m Telescope observations and data combination

As the ALMA observational data presented here lack sensitivities to the extended emission due to the central hole in the (u, v) -coverage ($< 5k\lambda$), the ALMA data were combined with zero-spacing data obtained using the NRO 45-m telescope. The 45-m observations were performed using the on-the-fly (OTF) observation mode during the winter seasons of 2008 and 2009. The scanning rates were set between $40''$ and $50'' \text{ s}^{-1}$, and data were sampled at a rate of 10 Hz, thereby providing a sufficient spatial sampling rate that met the Nyquist rate. The T100 receiver was used as a front-end, and the SAM45 spectrometers configured to cover a 512 MHz bandwidth with 1024 channels used as back-ends. Intensity calibration in the DSB antenna tempera-

ture (T_{λ}^*) scale was performed with the chopper-wheel method. The Hanning window function was applied to the spectrometer outputs to achieve Nyquist sampling in the frequency axis. To correct for the pointing offset, SiO (J=1–0) maser (42.821 and 43.122 GHz) sources were observed once every hour. Any data with pointing errors larger than $6''$ were excluded from the analysis.

The OTF data were processed with the NOSTAR software package (Sawada et al. 2008) to perform basic calibration procedures including baseline subtraction and application of main beam efficiency. Imaging was also obtained with NOSTAR by gridding data points to a $6''$ spacing grid and performing convolution with a spheroidal function (figure 1c). The total CO (1–0) luminosity detected within the field of view (FOV) of interferometric observations, defined as the region where the gain of the interferometric mosaic is above 0.9, is $4.3 \times 10^8 \pm 6.4 \times 10^6 \text{ K km s}^{-1} \text{ pc}^2$. We note that the denoted error is obtained by scaling the rms noise level in line free channels, and thus the uncertainty of the absolute temperature scale is not included. On the other hand, the luminosity detected by ALMA within the same area is $9.9 \times 10^7 \pm 5.7 \times 10^5 \text{ K km s}^{-1} \text{ pc}^2$. Thus, only approximately 23% of the CO flux was detected with the interferometric image synthesis.

2.3 Combined imaging

The the data sets taken with the different telescopes were combined by the procedure introduced in Kurono et al. (2009). The 45-m data cube was converted into pseudo visibility data sets using the same methodology as Hirota et al. (2014) to allow combined imaging and deconvolution with the data taken with ALMA. The relative weighting between the two data sets was optimized so that combined image achieves a similar resolution as the ALMA only data and also so that it recovers the total flux

detected by the 45-m observations. The calibrated ALMA visibility data and pseudo-visibility data generated from the 45-m observations were Fourier-transformed and deconvolved with the CLEAN method together. The parameters of the CLEAN beam are $2''.03 \times 1''.15$ ($44.3 \text{ pc} \times 25.1 \text{ pc}$) with a position angle of $\sim -77^\circ.7$. As described in §2.1, images were made for every two channels by averaging four neighboring channels; therefore the velocity resolution of the combined data is $\sim 2.54 \text{ km s}^{-1}$. The median value of the rms noise within the mapped area was $\sim 8.0 \text{ mJy}$ per beam. The combined data have a similar spatial distribution of noise as the ALMA-only data cube, with the 16th and 84th percentiles of the rms noise being 6.6 and 10.6 mJy per beam, respectively.

2.4 Ancillary data sets

To compare with the CO data, data sets of the star formation tracers were also prepared.

A catalog of H II regions was taken from Hirota et al. (2014) and was made by identifying H II regions from the $H\alpha$ image retrieved from the data archive of the Survey for Ionization in Neutral-Gas Galaxies (SINGG; Meurer et al. 2006) using the HIIphot software (Thilker et al. 2000). The resolution of the $H\alpha$ image is limited by a seeing of $1''.8$, which is comparable to the resolution of the CO data used here. Correction for foreground extinction was made by adopting $A_{H\alpha} = 0.18 \text{ mag}$, which is given by Meurer et al. (2006). Contamination of [N II] lines at rest wavelengths of 6548 \AA and 6583 \AA were also corrected by using the estimated fractional contribution of [N II] lines to the total bandpass, 0.11, which is given by Meurer et al. (2006). Application of these corrections resulted in scaling the original image by a factor of ~ 1.05 .

An image of $\text{Pa}\beta$ was produced from the narrow- and the broad-band filter images retrieved from the data archive of the HST/WFC3 ERS program (GO-11360). Continuum subtraction was achieved by subtracting the scaled broad-band image (F110W) from the narrow-band image (F128N).

3 GMC scale molecular gas distribution in M83

3.1 CO distribution

Figures 2(a) and 2(b) show maps of the integrated intensity and the peak temperature for ^{12}CO (1–0), respectively. Both of the CO maps were prepared from the combined CO (1–0) data cube presented in the previous section. The entire velocity range of the CO emission within the mapped region is approximately $350\text{--}630 \text{ km s}^{-1}$ and is much wider than the linewidths of individual molecular clouds which are several kilometers per second. Therefore, when generating the two-dimensional maps, a mask was applied to the original data cube to reject pixels with

low signal-to-noise ratios (SNRs). The mask was made by including all pixels with SNRs over 4 and also including pixels with SNRs over 2 and that are morphologically connected to the pixels with SNRs over 4. From the masked CO data cube, the first- and second-moment maps were also constructed (figures 2(c) and figure 2(d)). For reference, figure 3(a) also shows the contour map of the distribution of CO integrated intensity with annotations overlaid to indicate names of places that will be referred to hereafter.

The mapped region contains prominent galactic structures, including the stellar bar and the spiral arm that extends from the eastern end of the bar. The stellar bar in M83 lies at a position angle of $\sim 45^\circ$ and has a semi-major radius of approximately $84''$ (Hirota et al. 2014). The approximate extent of the stellar bar is indicated in figure 3 by the dotted line. The bar-to-arm transition region located around the eastern end of the bar was mapped by several studies in CO lines (e.g., Wiklind et al. 1990; Rand et al. 1999).

The spatial resolution ($44.3 \text{ pc} \times 25.1 \text{ pc}$) being comparable to the typical sizes of GMCs ($>20 \text{ pc}$; Sanders et al. 1985), the CO emission is resolved into many complex features. The spiral arm is resolved into many clumpy peaks that are arranged in arc-shaped ridges, and the bar is also arranged in ridges but with a more continuous distribution. The CO distribution in the arm and bar is narrow, in the sense that the widths are comparable to the beam size.

Along the leading sides of the bar, two continuous ridges of CO emission extend almost symmetrically with respect to the galactic center. The two molecular ridges correspond to 'offset ridges' commonly seen in molecular-rich barred-spiral galaxies (annotated in figure 3a). The offset ridges are found to be highly abundant in molecular gas. By assuming a CO-to- H_2 conversion factor of $2.0 \times 10^{20} \text{ cm}^{-2} (\text{K km s}^{-1})^{-1}$ (e.g., Bolatto et al. 2013), a correction factor of 1.36 for the existence of helium, and an inclination angle of 24° , the molecular gas surface density is found to be $\sim 200 M_\odot \text{ pc}^{-2}$ ($\sim 50 \text{ K km s}^{-1}$) at the eastern edge of the ridge, and it even increases to $\sim 800 M_\odot \text{ pc}^{-2}$ ($\sim 200 \text{ K km s}^{-1}$) or higher near the galactic center. These values are comparable to or even higher than the well-quoted typical surface density of Galactic GMCs ($\sim 170 M_\odot \text{ pc}^{-2}$; Solomon et al. 1987).

Near the eastern end of the bar, the molecular bar seen as a continuous ridge bifurcates into two molecular ridges that run through the leading and trailing sides of the spiral arm. The ridge on the leading side is brighter in CO compared to the one on the trailing side. Hereafter, we will refer to the ridge on the leading side as the 'primary arm ridge' and the one on the trailing side as the 'secondary arm ridge' (see figure 3a). Along the molecular ridges in the spiral arm, signatures of streaming motion can be recognized from the first-moment velocity map (figure 2c) with a velocity shift of $\sim 20 \text{ km s}^{-1}$. The existence

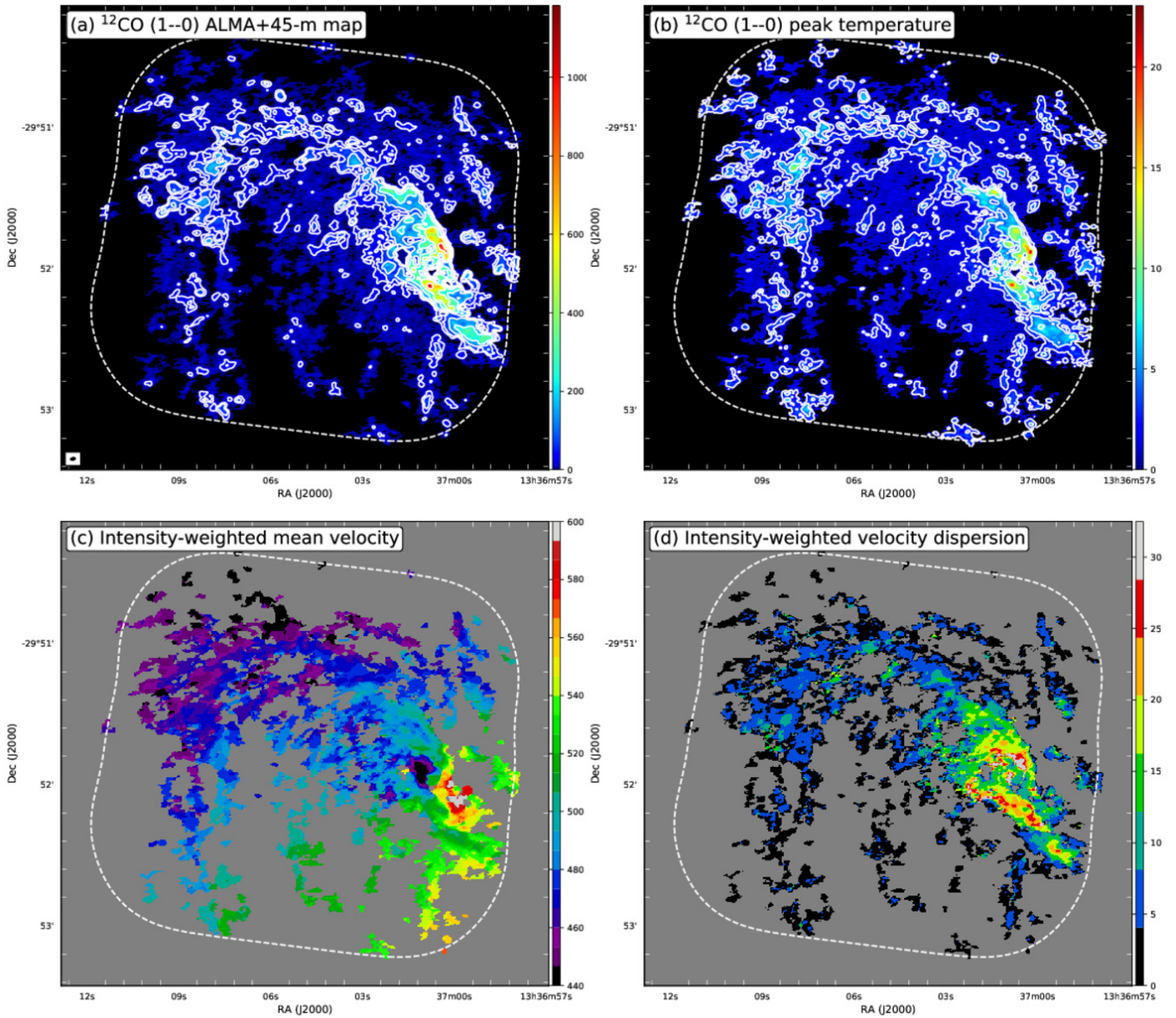


Fig. 2. (a) Velocity integrated intensity map of ^{12}CO (1-0) made from the combined data. Contour levels are 24, 48, 96, 192, 384, and 768 K km s^{-1} , respectively. The dashed line indicates the gain pattern of the mosaic observations at the normalized level of 0.9. The gain pattern is also indicated in each of the subsequent plots. Due to the application of the mask referred to in the main text, the rms noise of the integrated intensity image is not uniform. Typical rms values are ~ 1 and ~ 2 K km s^{-1} in the inter-arm and arm regions, respectively. (b) Peak temperature map for the combined ^{12}CO (1-0) data. Contour levels are 1.92, 3.84, and 7.68 K, respectively ($1\sigma = 0.32$ K). (c) Intensity-weighted mean velocity map of CO emission. (d) Intensity-weighted velocity dispersion map of CO emission.

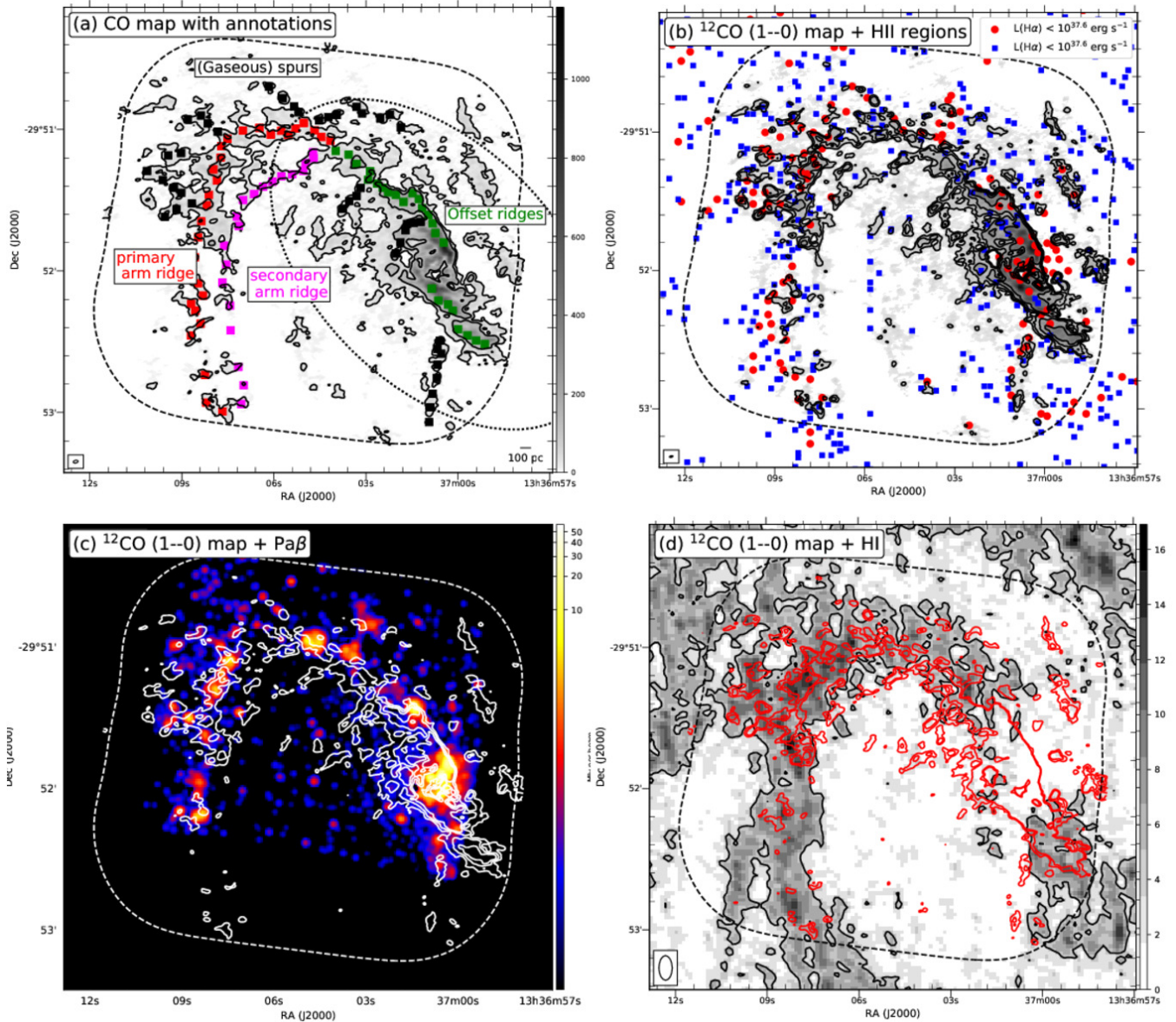


Fig. 3. (a) CO map overlaid with annotations to indicate the names of the places referred to in the text. (b) CO map compared with the distribution of H II regions. Red and blue markers indicate the location of H II regions with the uncorrected $\text{H}\alpha$ luminosity greater and lower than $10^{37.6} \text{ erg s}^{-1}$, respectively.

Contour levels are the same as in figure 2(a). (c) CO contours compared with $\text{Pa}\beta$ image in arbitrary units. The continuum-subtracted $\text{Pa}\beta$ image is smoothed to a resolution of $1''.8$ to align with that of the $\text{H}\alpha$ image used to identify the H II regions that are shown in (b). The contour levels are 33, 100, and 200 K km s^{-1} . (d) CO contours in red compared with H I map in units of $M_{\odot} \text{ pc}^{-2}$. The black contour is drawn at a level of $4 M_{\odot} \text{ pc}^{-2}$ for H I. The contour levels of the CO map are 30 and 60 K km s^{-1} .

of the velocity shift is in agreement with the finding made by Rand et al. (1999) and suggests that gas clouds in these two spiral arm ridges are subject to shock compression.

In addition to the ridges mentioned above, there exist secondary structures that extend with large opening angles from the primary arm ridge and the bar seen in CO (annotated in figure 3a). The secondary features extending from the primary arm ridge are on the leading side; they most likely correspond to the structures often seen in spiral arms and are referred to as 'spurs' or 'feathers' (e.g., Elmegreen 1980; La Vigne et al. 2006, hereafter, referred to as spurs). We note that the four outermost spurs indicated in figure 3(a) roughly coincide in position with the ones also identified by La Vigne et al. (2006) from an optical image. Unlike the spurs on the leading side of the primary arm ridge, some spurs that extend from the bar are on trailing side. The trailing spurs extending from a bar are often seen in other barred-spiral galaxies (Sheth et al. 2000; Zurita & Pérez 2008). The detailed mechanisms that produce the leading side spurs are still under active discussion, but most theories agree that gas clumps formed in an arm are sheared while moving toward the leading side of the arm (e.g., Wada & Koda 2004; Dobbs & Bonnell 2006; Renaud et al. 2013). On the other hand, the formation mechanism of the spurs on the trailing sides of a bar has not been investigated in detail. Except for the trailing spurs in the bar, most of the spurs on the leading side are closely associated with H II regions. Active star formation in spurs is in agreement with the suggestion that spurs, possibly produced from bound gas clumps, are preferred sites for star formation (e.g., Schinnerer et al. 2017).

3.2 Comparison with tracers of high mass star formation

Figures 3(b) and 3(c) compare the CO map with the distribution of the H II regions and a map of $Pa\beta$ emission, respectively. Comparing the distribution of CO emission with the tracers of massive star formation, the SFE in molecular clouds does not appear to be uniform within the region observed. A large number of H II regions are found in limited areas such as the primary arm ridge, spurs that extend toward the leading side of the primary ridge, and around the galactic center. On the other hand, it is evident that fewer H II regions are found along the secondary arm ridge and in the inter-arm region located on the trailing side of the bar. Later in §5, we will quantitatively investigate the SFE for individual GMCs. Further in §6, we will discuss whether the apparent regional variation in star formation activity is caused by intrinsic variations in the SFE in GMCs.

3.3 Comparison with the distribution of atomic hydrogen

Figure 3(d) compares the CO map with a map of the atomic hydrogen (HI) retrieved from the archive of The HI Nearby Galaxy Survey (THINGS; Walter et al. 2008), which is an imaging survey of HI in nearby galaxies made with the Very Large Array (VLA). The archival image was made with robust weighting of the visibilities and the size of the synthesized beam is $10''.4 \times 5''.6$. By assuming optically thin emission of HI, we converted the unit of the HI image into surface density which resulted in a sensitivity of $\sim 0.3 M_{\odot} \text{pc}^{-2}$.

Over the FOV of the CO observation, the surface density of HI is at most $12 M_{\odot} \text{pc}^{-2}$, and is well below that of molecular gas. As HI is suggested to have a smooth distribution even at small spatial scales (finer than 100 pc; Leroy et al. 2013), we assume that the surface density of HI is still well below that of molecular gas even when compared at the scale of GMCs.

Another concern might be the missing flux of the HI image. As the THINGS HI image is not sensitive to structures larger than $15'$ (~ 20 kpc) due to the lack of short spacing baselines, the contribution of the missing flux might be a concern. From a comparison of the HI flux detected by VLA observations with single dish telescope observations, Crosthwaite et al. (2002) estimated that large-scale features greater than $15'$ in M83 could have a mean surface HI density of $2 \pm 0.5 M_{\odot} \text{pc}^{-2}$. Although the data used by Crosthwaite et al. (2002) and those presented as part of THINGS survey are not identical, the total HI flux detected in the two data sets do not differ greatly from each other (480 Jy km s^{-1} vs. 360 Jy km s^{-1}). Therefore, we hereafter assume that the contribution of HI is not significant compared to the molecular gas, and do not take the HI gas content into account in the following analyses.

On the basis of the spatial distribution of CO and HI in spiral arms, several authors suggested that in the molecular dominated part of the galactic gas disks, HI is preferentially found in star-forming regions as the product of photo-dissociation (M51 by Rand et al. 1992; the MW by Koda et al. 2016). For the particular case of the eastern spiral arm of M83, Rand et al. (1999) compared their interferometric CO map with the HI map of Tilanus & Allen (1993). They noted that it is difficult to identify systematic spatial offsets between HI and CO peaks which were taken as evidence for HI being the photo-dissociation product in M51 (Rand et al. 1992). However, we note that the previous CO map of M83 obtained by Rand et al. (1999) has missed the secondary arm ridge and the arm traced by the HI emission is more aligned with the primary arm ridge compared to the secondary one, although the beam size of the HI image is considerably larger than that of the CO image. As the SFE is suggested to be lower in the secondary arm ridge compared to the primary arm ridge, the notion of HI as the photo-dissociation product seems to still hold in the eastern arm of M83.

4 Properties of GMCs

4.1 Cloud identification

GMCs are identified from the three-dimensional ^{12}CO (1–0) data. Before performing the cloud identification, the original data cube is smoothed spatially by convolving with a Gaussian beam to obtain an axisymmetric beam profile of $2''.1$ (~ 46 pc). The 16th, 50th, and 84th percentiles of the rms noise are 7.3, 10.6, and 13.7 mJy per beam with a velocity resolution of ~ 2.54 km s $^{-1}$. We used the *astrodendro*¹ software package to identify clouds from the data cube. Although the software can identify hierarchically nested sets of topologically closed surfaces, we have adopted only closed surfaces with the finest spatial scales, which are commonly referred to as *leaves*. The reason for using only *leaves* is that a resolution of ~ 46 pc does not resolve the typical size of GMCs, because of which *leaves* should not represent substructures inside GMCs. Instead, each of them should correspond to an individual GMC or a complex of GMCs that are closely packed within a resolution limit.

Parameters for the cloud decomposition algorithm are configured such that each *leaf* has a peak SNR over 3, and the peak SNR of each *leaf* is higher by at least 3 from the merging level to neighboring *leaves*. In addition, to avoid picking up small features that could be mere noise fluctuations, we discarded *leaf* candidates where the number of pixels occupied in the three-dimensional data cube is below $3 \times (A_{\text{beam}}/A_{\text{pixel}})$, where A_{beam} and A_{pixel} are the areas of the beam and a pixel. We also tried a threshold value of $2 \times (A_{\text{beam}}/A_{\text{pixel}})$, which appears more plausible considering the factor-of-2 oversampling used in the velocity direction in the data cube (§2.3). However, we discarded it because while the number of identified *leaves* increased by approximately 6%, some of the newly detected *leaves* are smaller than the beam size and thus are too small for the size parameters to be correctly determined later in §4.2.

With the adopted set of parameters, GMCs with a peak SNR down to 6 which corresponds to ~ 1.4 K, are expected to be detected. Assuming that a minimum detectable GMC has a Gaussian profile with a radius and linewidth of 46 pc and 5 km s $^{-1}$, respectively, and also adopting the 'standard' CO-to-H $_2$ conversion factor (see §4.2.1), the mass threshold for the GMC identification is estimated to be $2.3 \times 10^5 M_{\odot}$. We will see later in §4.7 that the mass threshold estimated here is consistent in regions where molecular clouds are not closely packed. On the other hand, in regions with high average molecular gas density, such as the bar and the central region, the detection limit is elevated to around $10^6 M_{\odot}$; this point will also be reviewed in §4.7.

All the identified *leaves* are checked by examining the two-dimensional distribution obtained by projecting each on the x - y plane. After manually flagging three *leaves* with too dispersed

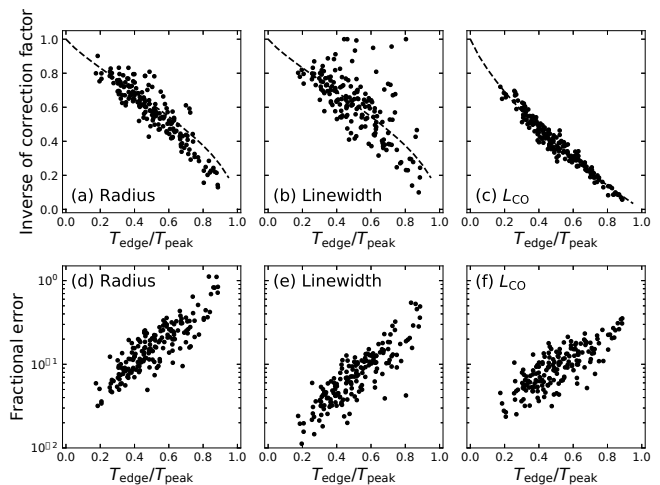


Fig. 4. (a–c) Ratio of the extrapolated value to unextrapolated value for size, velocity dispersion, and CO luminosity, respectively, as a function of $T_{\text{edge}}/T_{\text{peak}}$. (d–f) Fractional uncertainty for each quantity in (a–c) as a function of $T_{\text{edge}}/T_{\text{peak}}$. Note that the ordinate in each plot is in logarithmic scale.

appearance, 179 *leaves* remained. We regard each *leaf* as the 'kernel' of a GMC because the surface boundary determined by each *leaf* does not extend to the 0 K level and thus traces just a limited volume around the peak of each GMC.

4.2 Derivation of basic cloud parameters

The centroid position and the velocity of each GMC are derived by calculating the intensity-weighted first moment within each GMC kernel. The maximum temperatures within each GMC kernel are taken as peak temperatures (T_{peak}), and we also record the minimum temperature as the edge temperature (T_{edge}).

Two-dimensional root-mean-square sizes and the velocity dispersion of each GMC (σ_x , σ_y , and σ_v , where $\sigma_x > \sigma_y$) are derived by calculating second moments in three axes within each kernel mask. The second-moment value calculated within each kernel mask is extrapolated to the 0 K level by following the procedure proposed by Rosolowsky & Leroy (2006), which calculates a moment value with various temperature thresholds in the range between T_{edge} and T_{peak} and linearly extrapolates it to the 0 K level. The extrapolated second moments are further corrected by subtracting the resolution element size in quadrature to account for the finite resolution.

The CO luminosity of the cloud is first calculated within each GMC kernel and then corrected by applying the same extrapolation method as for the size parameters.

The three plots in the top row of figure 4 show the ratio of the extrapolated value to the unextrapolated value for size ($\propto \sqrt{\sigma_x \sigma_y}$), velocity dispersion, and CO luminosity, respec-

¹ <http://www.dendrograms.org>

tively, as a function of the ratio of T_{peak} to T_{edge} . The dashed line in each plot indicates the expected behavior with a simple Gaussian profile. We see in each plot that most of the data points for the identified GMCs agree with the expected line for a Gaussian profile.

Uncertainties for the size parameters and CO luminosity are determined by performing bootstrap error estimates. As shown by the three plots in the bottom row of figure 4, the uncertainty assigned to each GMC quantity depends on $T_{\text{peak}} / T_{\text{edge}}$. As we will see later in §4.5.1, some GMCs in the center and the bar have a low contrast to their ambient regions—i.e., $T_{\text{edge}} / T_{\text{peak}}$ is high—and thus those GMCs are assigned a larger uncertainty for cloud parameters compared to the GMCs in uncrowded regions.

4.2.1 Adopted definition of physical quantities

After determining the rms size values and the CO luminosity for each cloud, those values are mapped to physical quantities. The linewidth of the cloud (ΔV) is simply taken as $\Delta V = \sqrt{8 \log 2} \sigma_v$. The effective size of the cloud (R) is defined as

$$R = \frac{3.4}{\sqrt{\pi}} \sqrt{\sigma_x \sigma_y}, \quad (1)$$

where $3.4/\sqrt{\pi}$ is an empirical factor that is determined by Solomon et al. (1987).

The molecular gas mass for each GMC (M_{GMC}) is calculated from the CO luminosity (L_{CO}) by applying the CO-to- H_2 conversion factor of $2.0 \times 10^{20} \text{ cm}^{-2} (\text{K km s}^{-1})^{-1}$, which is considered to be valid for the inner disk of massive spiral galaxies (Bolatto et al. 2013) along with a correction factor of 1.36 that accounts for the contribution of helium and other elements:

$$\left(\frac{M_{\text{GMC}}}{M_{\odot}} \right) = 4.4 \left(\frac{L_{\text{CO}}}{\text{K km s}^{-1} \text{ pc}^2} \right). \quad (2)$$

The virial mass is calculated with the following equation which neglects the magnetic energy and external pressure,

$$M_{\text{vir}} = \frac{1}{a_1} \frac{5R\sigma_v^2}{G}, \quad (3)$$

where G is the gravitational constant, and a_1 is a factor that encapsulates the effects of the density distribution. The factor, a_1 , can be written as $a_1 = (1 - n/3) / (1 - 2n/5)$ for a cloud that follows the power law density profile of $\rho(r) \propto r^{-n}$ (Bertoldi & McKee 1992). Hereafter, we employ $n=1$ (Solomon et al. 1987).

The virial parameter (Bertoldi & McKee 1992), which is a measure of the ratio of the kinetic to gravitational energy of a GMC, is defined as

$$\alpha_{\text{virial}} \equiv M_{\text{vir}} / M_{\text{GMC}}. \quad (4)$$

The Average gas surface density of GMC (Σ_{GMC}) is defined as

$$\Sigma_{\text{GMC}} = M_{\text{GMC}} / (\pi R^2). \quad (5)$$

The volume density is calculated with the following equation taken from Leroy et al. (2015):

$$\rho_{\text{GMC}} = 1.26 M_{\text{GMC}} / \left((4/3) \pi R^3 \right) \quad (6)$$

The free-fall time (τ_{ff}) of GMC is calculated as follows:

$$\tau_{\text{ff}} = \sqrt{\frac{3\pi}{32G\rho_{\text{GMC}}}}. \quad (7)$$

4.3 Distribution of identified GMCs

Figure 5 shows the distribution of the identified GMCs. The spatial extent of each GMC is displayed by an ellipse with major and minor radii of $3.4/\sqrt{\pi} \sigma_x$ and $3.4/\sqrt{\pi} \sigma_y$, respectively. The sum of the GMC mass derived by applying the extrapolation method and the CO conversion factor described in the previous section is $\sim 5.6 \times 10^8 M_{\odot}$, which is approximately 33% of the total molecular gas mass within the target region ($\sim 1.7 \times 10^9 M_{\odot}$). The fractional molecular gas mass identified as GMC is comparable to the value found in M51 ($\sim 54\%$, Colombo et al. 2014) with a similar spatial resolution.

4.4 Definition of environmental masks

To investigate the regional variation in the properties of GMCs, we define regional masks indicated in figure 6. The area within the galactocentric radius of $16''$ ($\sim 350 \text{ pc}$) is defined as the central region to include a gas ring with a radius of $\sim 9''$ (Elmegreen et al. 1998) and condensations of molecular gas formed at the crossing points of the ring and the bar offset set ridges (e.g., Sakamoto et al. 2004). Two rectangles that cover the offset ridges of the molecular bar are defined as the bar region. Two inter-arm regions are defined at the leading and trailing sides of the bar, respectively. The arm region is defined to cover the two spiral arm ridges and associated spurs that extend toward the leading side. Within the arm region, we also define two subregions that trace the spiral arm ridges described in §3.1, i.e., the primary and secondary arm ridges.

4.5 Environmental variation in GMC properties

In this subsection, we investigate the environmental variation in GMC properties by examining the statistical distribution of each quantity. We employ a box-and-whisker plot to display the quartiles of each quantity, as Colombo et al. (2014) used for M51. Table 2 also tabulates the 25th, 50th, and 75th percentiles of relevant GMC properties, including the peak temperature (T_{peak}), edge temperature (T_{edge}), size (R), linewidth (ΔV), cloud mass (M_{GMC}), gas surface density (Σ_{GMC}), virial parameter (α_{virial}), and free-fall time (τ_{ff}) of the GMCs in each regional mask.

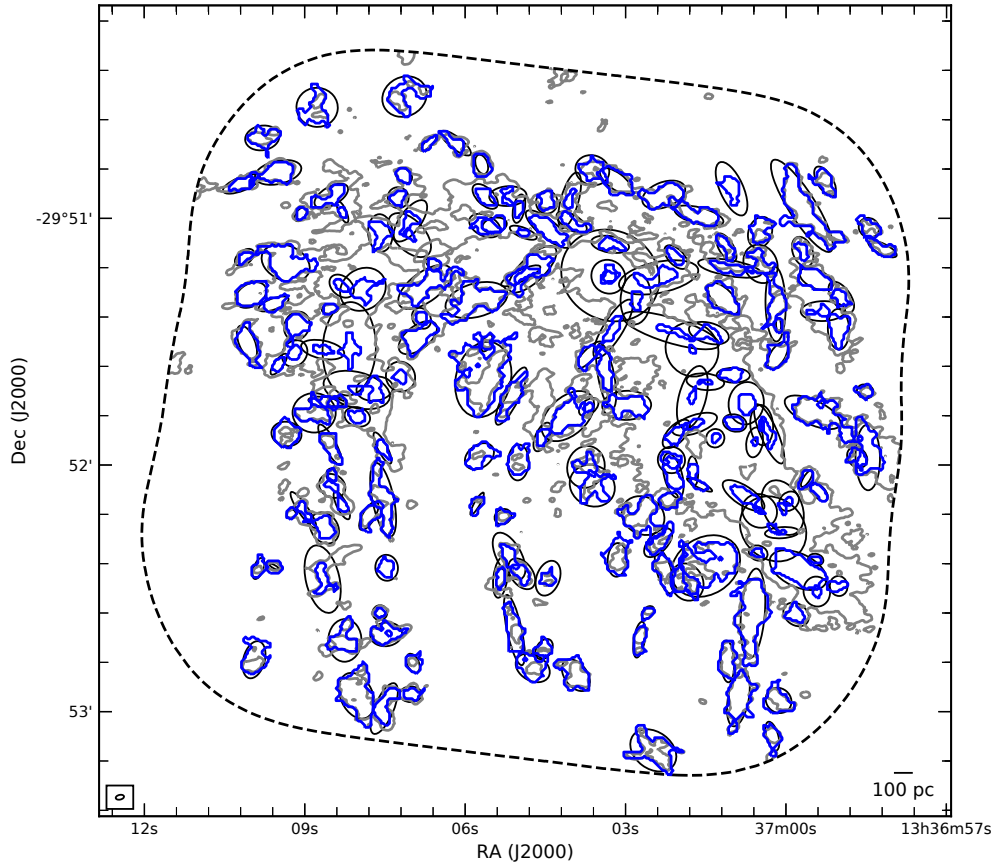


Fig. 5. Distribution of the identified GMCs overlaid on the CO map indicated with a contour line with 13 K km s^{-1} level (gray line). Each ellipse indicates the position and the effective major and minor radii of a GMC (i.e. $3.4/\sqrt{\pi} \sigma_x$ and $3.4/\sqrt{\pi} \sigma_y$). The solid blue line indicates the boundary of the kernel for each GMC projected on the $x - y$ plane.

Table 2. Properties of identified GMCs

	N	T_{peak} (K)	T_{edge} (K)	R (pc)	ΔV (km s^{-1})	M_{GMC} ($10^6 M_{\odot}$)	Σ_{GMC} ($M_{\odot} \text{ pc}^{-2}$)	α_{virial}	τ_{ff} (Myr)
all	179	$3.3^{+1.4}_{-0.8}$	$1.6^{+0.6}_{-0.5}$	69^{+20}_{-16}	$13.3^{+5.1}_{-3.9}$	$1.6^{+1.7}_{-0.8}$	106^{+71}_{-40}	$1.4^{+0.9}_{-0.5}$	$6.4^{+2.9}_{-1.6}$
Inter-arm (trail)	42	$2.3^{+0.7}_{-0.3}$	$1.0^{+0.3}_{-0.2}$	72^{+21}_{-15}	$12.6^{+5.3}_{-4.0}$	$1.2^{+1.6}_{-0.5}$	80^{+24}_{-26}	$1.8^{+0.9}_{-0.7}$	$8.6^{+1.5}_{-2.6}$
Inter-arm (lead)	27	$3.0^{+0.8}_{-0.6}$	$1.2^{+0.1}_{-0.1}$	72^{+14}_{-15}	$12.6^{+3.9}_{-1.9}$	$1.1^{+1.4}_{-0.3}$	95^{+68}_{-43}	$1.8^{+0.9}_{-0.6}$	$6.8^{+3.4}_{-0.8}$
Arm	66	$3.8^{+1.0}_{-1.1}$	$1.7^{+0.8}_{-0.6}$	62^{+20}_{-14}	$11.9^{+3.5}_{-2.9}$	$1.5^{+1.6}_{-0.8}$	123^{+50}_{-43}	$1.0^{+0.5}_{-0.4}$	$6.0^{+1.8}_{-1.2}$
Arm ridge (secondary)	15	$3.2^{+0.6}_{-0.7}$	$1.6^{+0.1}_{-0.5}$	64^{+21}_{-13}	$9.8^{+3.5}_{-1.3}$	$1.3^{+1.7}_{-0.7}$	113^{+24}_{-31}	$1.1^{+0.3}_{-0.5}$	$6.7^{+1.8}_{-1.0}$
Arm ridge (primary)	21	$4.1^{+1.3}_{-1.3}$	$2.1^{+1.6}_{-1.0}$	74^{+29}_{-19}	$12.3^{+4.1}_{-3.9}$	$1.7^{+1.1}_{-0.8}$	101^{+52}_{-47}	$1.1^{+0.5}_{-0.3}$	$6.7^{+4.7}_{-1.0}$
Bar	17	$5.2^{+2.4}_{-0.9}$	$3.9^{+2.1}_{-0.7}$	76^{+55}_{-16}	$18.7^{+17.1}_{-4.5}$	$4.2^{+4.1}_{-2.3}$	142^{+209}_{-38}	$1.6^{+2.1}_{-0.5}$	$6.0^{+2.5}_{-2.5}$
Center	13	$9.8^{+2.7}_{-5.6}$	$5.6^{+3.0}_{-2.9}$	77^{+10}_{-25}	$29.5^{+20.3}_{-9.9}$	$5.9^{+5.0}_{-3.8}$	411^{+538}_{-184}	$1.7^{+1.0}_{-0.4}$	$3.0^{+0.9}_{-0.6}$

Each GMC property is noted as M_{D25}^{D75} , where M , $D25$, and $D75$ are median, the distance to the 25th percentile from the median, and the distance to the 75th percentile from the median of the number distribution, respectively.

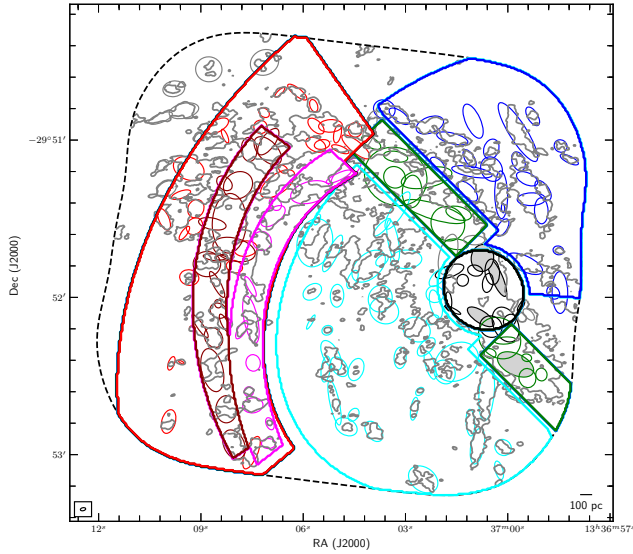


Fig. 6. Definition of the environmental mask indicated with heavy solid lines, overlaid on the distribution of GMCs (ellipses in thin line) and on the CO map (gray contour). The central region, the bar, inter-arm (trailing side), inter-arm (leading side), the arm, the primary arm ridge, and the secondary arm ridge are defined and indicated with black, green, cyan, blue, red, dark-red, and magenta, respectively. The four gray-shaded ellipses indicate the four most massive clouds, which appear as outliers in the plots of mass spectra (will be discussed later in §4.7).

4.5.1 Variation in basic properties

Many of the GMC properties are dimensionally proportional to combinations of three parameters, namely, the temperature, the size, and the linewidth. Therefore, we start by examining the distribution of these quantities before investigating other properties.

Figures 7 (a)-(c) show the environmental variation in the peak temperature (T_{peak}), effective size (R), and linewidth (ΔV), respectively. The median peak temperature of the identified clouds is approximately 3.3 K above the background emission, suggesting that most of the clouds in our sample are marginally resolved at the 46 pc spatial resolution. There is environmental variation in the peak temperature. By examining the range of the 25th and 75th percentiles for T_{peak} in each region, the peak temperature is found to exhibit regional variations and is highest in the center (4.2–12.5 K), followed by the bar (4.3–7.6 K), arm (2.7–4.8 K), and inter-arm regions (2.0–3.0 K and 2.4–3.8 K for trailing and leading sides, respectively). Even within the arm region, there is a variation in the peak temperature: T_{peak} in the primary arm ridge extends to a higher regime (2.8–5.4 K) compared to the secondary one (2.5–3.8 K). In addition to T_{peak} , the linewidth also follows a similar trend, although the difference between the inter-arm and the arm is moderate.

On the other hand, the effective size of the clouds does not

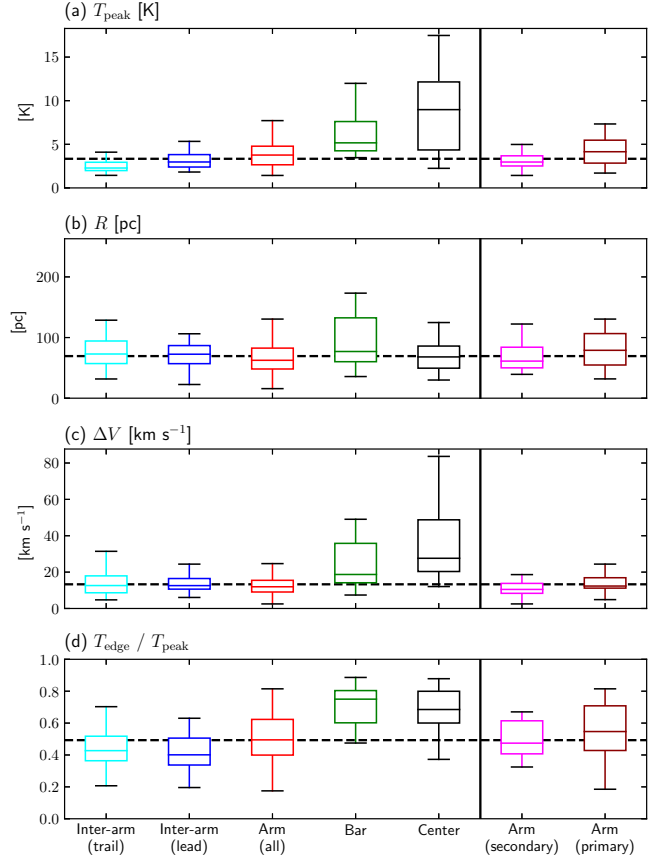


Fig. 7. Box-and-whisker plots for (a) peak temperature (T_{peak}), (b) effective radius (R), (c) linewidth (ΔV), and (d) edge-to-peak temperature ratio ($T_{\text{edge}}/T_{\text{peak}}$). Upper and lower edges of each box indicate 25th (Q1) and 75th (Q3) percentiles of the number distribution. Upper whisker extends up to the last data point less than $Q3 + 1.5\text{IQR}$, where IQR is the interquartile range ($= Q3 - Q1$). Lower whisker extends down to the last data point greater than $Q1 - 1.5\text{IQR}$. Data points outside the whiskers are indicated with pluses. Median value is indicated with a horizontal line within each box. Dashed horizontal line indicates the median value for all samples.

clearly follow the same trend. The only notable variation is that clouds in the bar region are larger than the others and there is little variation in the size parameters among other regions. The lack of strong variation in the size parameter is not unforeseeable, because the cloud partition algorithm tends to divide cloud emission into structures with rather uniform size scale that is comparable to the beam size (Hughes et al. 2013).

Figure 7(d) shows the ratio of the edge-to-peak temperatures of clouds ($T_{\text{edge}} / T_{\text{peak}}$). The higher this value is for a GMC, the less distinct the cloud becomes from its surroundings. The median value for the entire sample is approximately 0.49, and thus most of the identified GMCs are not well isolated from their environment. In particular, GMCs in the bar and the center exhibit quite elevated values (0.6–0.8 for 25th to 75th percentile range). As this quantity primarily determines the uncertainties

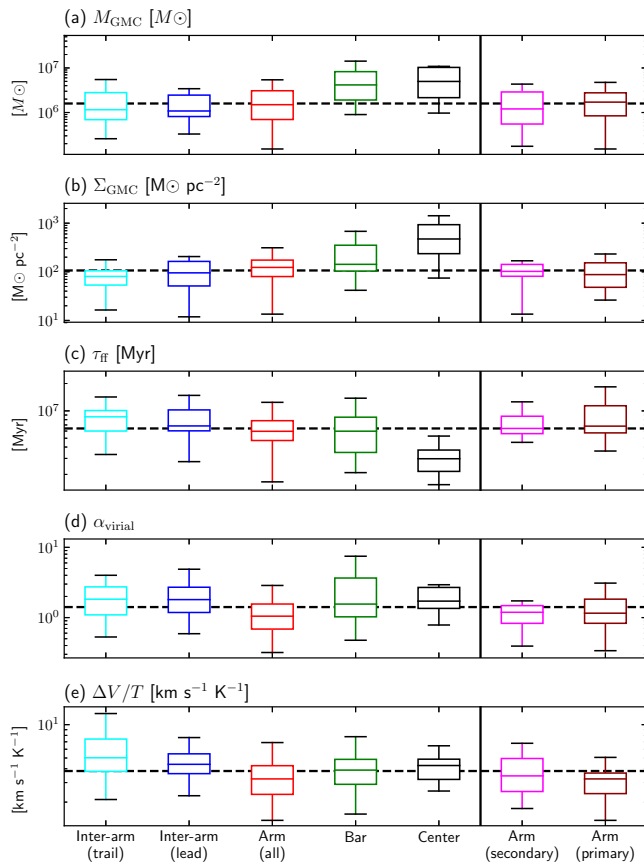


Fig. 8. Same as figure 7, but for (a) cloud mass (M_{GMC}), (b) average surface density (Σ_{GMC}), (c) free-fall time (τ_{ff}), (d) virial parameter (α), and (e) $\Delta V/T_{\text{peak}}$, respectively.

assigned to each cloud parameter (as seen in figure 4), GMC properties in the center and the bar regions are more uncertain compared to the GMCs in other regions.

4.5.2 Variation in derived properties

Here, we look into the statistical distribution of the cloud mass (M_{GMC}), gas surface density (Σ_{GMC}), free-fall time (τ_{ff}), and virial parameter (α_{virial}). Box-and-whisker plots for these parameters are presented in figure 8. These four quantities have a dimensional dependence on the combinations of three quantities, temperature (T), linewidth (ΔV), and cloud size (R) as follows:

$$\begin{aligned}\Sigma_{\text{GMC}} &\propto T\Delta V, \\ M_{\text{GMC}} &\propto T\Delta VR^2, \\ \tau_{\text{ff}} &\propto (T\Delta V/R)^{-1/2}, \\ \alpha_{\text{virial}} &\propto \Delta V/(TR).\end{aligned}$$

The median value of Σ_{GMC} for all samples is $\sim 106 M_{\odot} \text{pc}^{-2}$ and is close to the values found in the Galactic GMCs (80–120

$M_{\odot} \text{pc}^{-2}$; Heyer et al. 2009). Σ_{GMC} is highest in the central region with lower and upper quartiles of ~ 230 and $\sim 950 M_{\odot} \text{pc}^{-2}$, respectively. The bar region also exhibits elevated values of Σ_{GMC} with lower and upper quartiles of ~ 100 and $\sim 350 M_{\odot} \text{pc}^{-2}$, respectively. The environmental variation expressed by the fact that Σ_{GMC} is higher in the center and the bar is easily understood considering the dimensional dependence of Σ_{GMC} on $T\Delta V$.

The cloud mass, M_{GMC} , shows a similar trend as Σ_{GMC} . This is also comprehensive because M_{GMC} has an extra dependence on R^2 compared to Σ_{GMC} , and R does not exhibit strong regional variation.

The median value of the free-fall time, τ_{ff} , for all clouds is 6.4 Myr. It is shortest in the central region with lower and upper quartiles of 2.4 and 3.9 Myr, respectively. As τ_{ff} is proportional to the inverse square of $T\Delta V$, the shorter τ_{ff} in the central region is reasonable.

The virial parameter, α_{virial} , has a median value of ~ 1.4 for all samples. It tends to be smaller in the arm (median value is ~ 1.0) compared to other regions including the inter-arm, bar, and center (median value is ~ 1.8). As it is dimensionally proportional to $\Delta V/(TR)$ and as R does not exhibit strong regional variation except for the bar, an environmental variation of $\Delta V/T$ is expected to be mainly responsible for the variation in α_{virial} . Figure 8(e) shows the distribution of $\Delta V/T_{\text{peak}}$. At least for the difference between the inter-arm regions and the arm region, the distribution of $\Delta V/T_{\text{peak}}$ is in agreement with the expectation.

4.6 Scaling relations

Early studies of Galactic molecular clouds have revealed the existence of scaling relations between the cloud properties, which are often referred to as Larson’s three laws (Larson 1981; Solomon et al. 1987): (1) velocity dispersion of the cloud has a power-law dependence on the cloud size, $\sigma_v \propto R^{\beta}$, with an index β of approximately 0.5; (2) the virial mass of the cloud is close to the luminosity mass ($M_{\text{vir}} \simeq M_{\text{GMC}}$); and (3) the average volume density of the cloud is nearly inversely proportional to the cloud size ($\rho_{\text{GMC}} \propto R^{-1}$), or in other words, the average surface density is almost constant among GMCs. In reality, only two of these three laws are independent because if two of them are provided, then the remaining one can be algebraically derived from the two laws. Therefore, we examine the first two of Larson’s laws with the GMCs in M83.

4.6.1 Linewidth–size relation

Figure 9(a) shows the linewidth–size relation for all GMC samples, and (b)–(h) show the same relation for each subregion. For reference, figure 9(i) plots Galactic GMC samples from Solomon et al. (1987). The linewidth–size relation given by

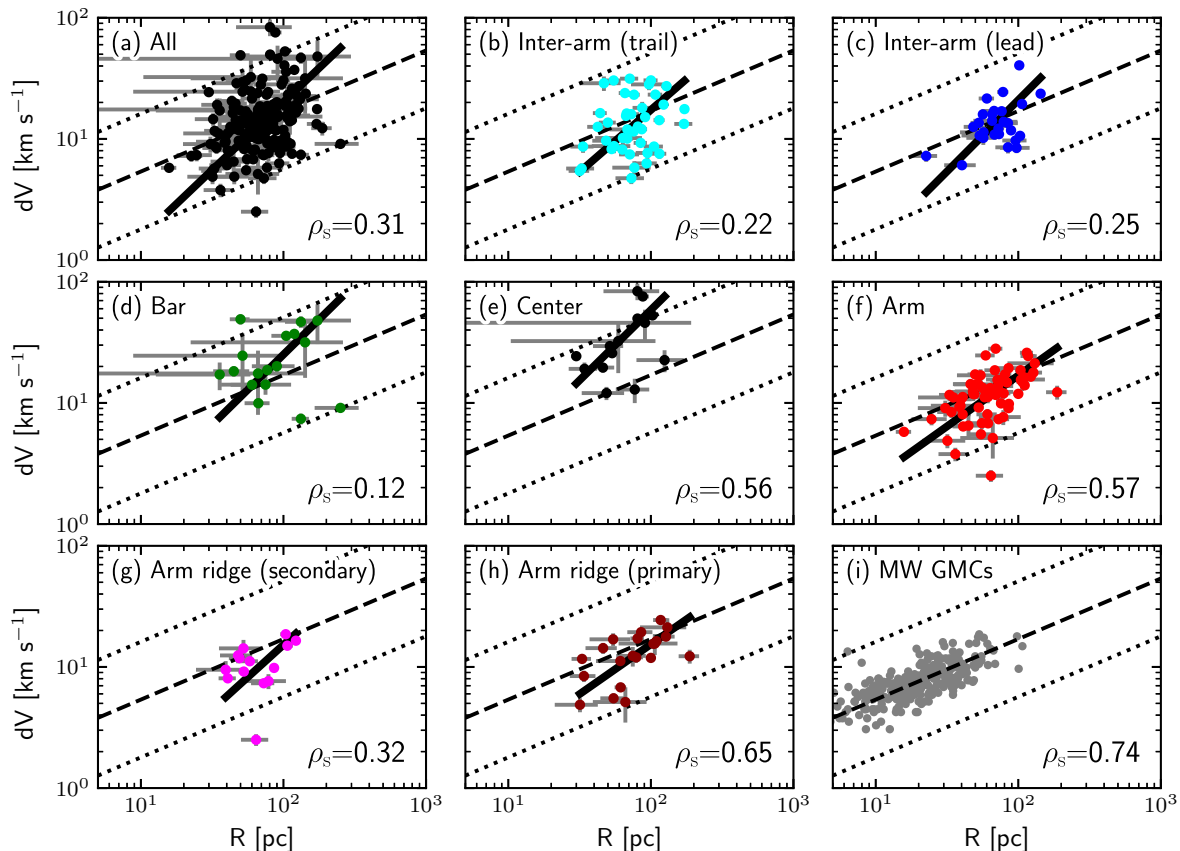


Fig. 9. (a) Linewidth–size relationship for all the GMC samples in M83. (b–h) Same as (a), but for each subregion defined in figure 6. (i) Same as (a), but for Galactic clouds (Solomon et al. 1987) and M51 clouds (Colombo et al. 2014) indicated with gray and purple markers, respectively. In each plot, the dashed line indicates the fit to Galactic GMCs given by Solomon et al. (1987), $\Delta V \sim 1.70 R^{0.5}$, and the two dotted lines show $\times 3$ and $1/3$ of it, respectively. Spearman’s rank correlation coefficient (ρ_s) is noted at the bottom right corner of each plot. Black solid lines indicate the power-law fitting results for the GMCs in M83.

Solomon et al. (1987) is plotted with a dashed line in each plot. In each plot, Spearman’s rank correlation coefficient (ρ_s), a non-parametric measure of a rank correlation coefficient, is given to indicate the degree of correlation. We regard a value of ρ_s greater than 0.7 as a sign of significant correlation. Data points in each plot are fitted with a power-law relation by minimizing the effective variance (Orear 1982), and the fitted result is overplotted.

If all the GMC samples are taken together, it is difficult to identify a sign of the existence of correlation (figure 9a). The calculated ρ_s is approximately 0.3, and this is quite low compared to the value found from the Galactic GMCs ($\rho_s \sim 0.7$). Even with division into subregions, the apparent lack of correlation is also the same, supported by the low value of ρ_s (figure 9b–h). We will shortly discuss why we observed a weaker correlation for the linewidth–size relation in M83 compared to the MW samples of Solomon et al. (1987) in §4.6.3.

4.6.2 Relationship between virial mass and CO luminosity

Figure 10 shows the relationship between the virial mass and CO luminosity for the GMCs in M83. In each plot, the line representing the equality of the virial mass and the luminosity mass calculated from equation 2 is overplotted.

Contrary to the low correlation found for the linewidth–size relation, the GMCs in M83 are mostly in agreement with Larson’s second law. This is consistent with the narrow range of α_{virial} , lower and upper quartiles being 0.9 and 2.3 for all samples, seen in the previous subsection. Also, the power-law fitting resulted in almost linear relations for all of the subregions considered here. Correlation coefficients, ρ_s , fall in the range between 0.70 and 0.89 and support the apparent existence of the significant correlation.

4.6.3 Why the observed linewidth–size relation exhibits weak correlation?

Among the three Larson’s laws, the linewidth–size relation has attracted particular attention because the similarity of its form

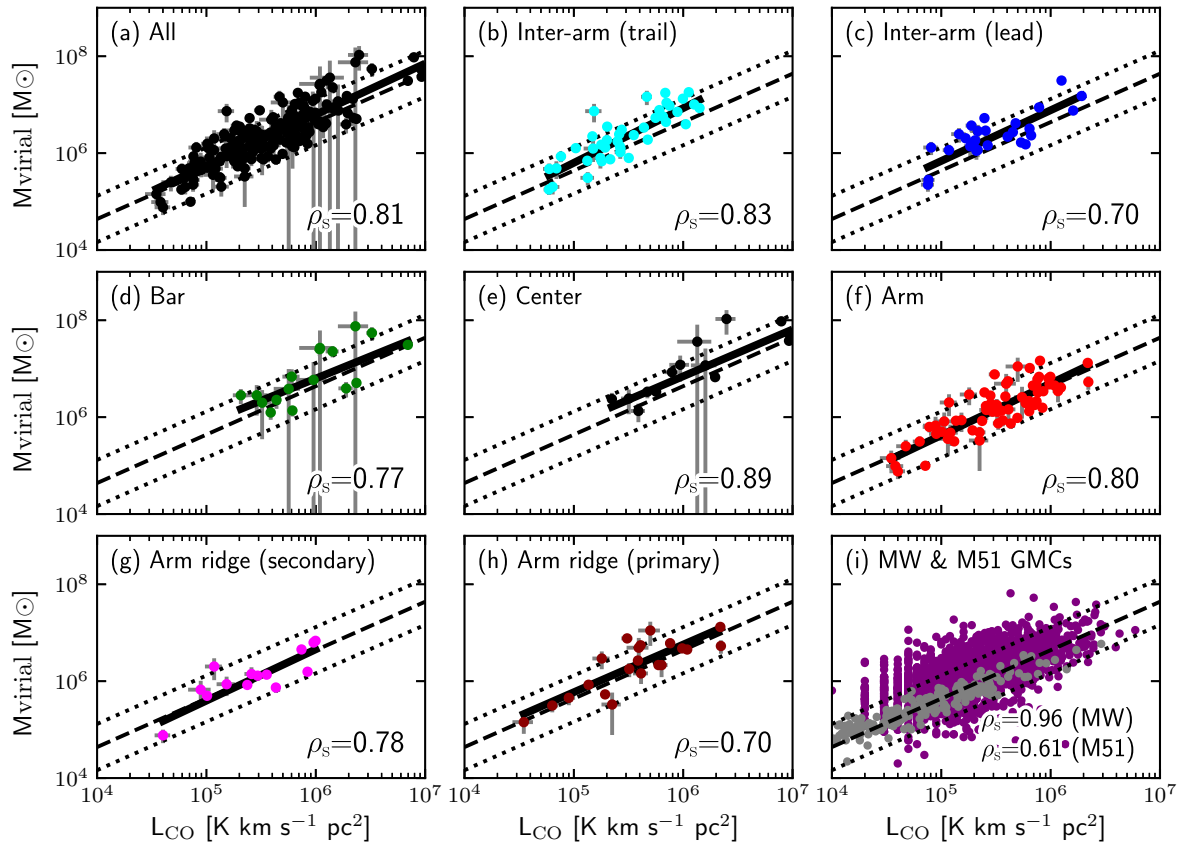


Fig. 10. Same as figure 9, but for the relationship between virial mass and CO luminosity. The Dashed line in each plot indicates that the line for the virial mass is equal to the cloud mass derived with equation 2, and two dotted lines indicate $\times 3$ and $1/3$ of it, respectively.

with the Kolmogorov cascade, which happens for incompressible turbulence, is considered to be the manifestation of the hierarchical nature of GMC which is governed by the turbulent motion (Larson 1981). The tight correlation between the linewidth and size in Galactic clouds found by Solomon et al. (1987) and the similarity of the internal structure function of GMCs studied by Heyer & Brunt (2004) are taken as evidence for the universality of the linewidth–size relation. However, later with the updated dataset, Heyer et al. (2009) pointed out that the coefficient of the linewidth–size relation ($\sigma_{v,0}$) is in reality not uniform, but it depends on the surface density (Σ_{gas}) of the cloud as follows,

$$\sigma_{v,0} (= \sigma_v / R^{1/2}) \propto \Sigma_{\text{gas}}^{1/2}. \quad (8)$$

Heyer et al. (2009) also pointed out that this $\sigma_{v,0}$ – Σ_{gas} relation is mathematically equivalent to Larson’s second law, which is also equivalent to $M_{\text{vir}} = M_{\text{GMC}}$ if the assumed CO-to- H_2 conversion factor is correct.

The weak correlation observed for the linewidth–size relation with a ρ_s of approximately 0.3 (§4.6.1) should partly be attributed to the fact that the GMC samples adopted here have a limited dynamic range, in particular for the size parameter (§4.5.1). In addition to the limited dynamic range, the relatively

large uncertainty associated with the cloud properties seen in figure 4 could be responsible for the weak correlation of the linewidth–size relation.

However, the firm correlation observed between the virial mass and CO luminosity (§4.6.2) implies that the variation in the surface density is yet another factor that contributes to the weak correlation of the linewidth–size relation, as pointed out by Heyer et al. (2009). Figure 11 plots the square of the linewidth–size relation coefficient as a function of the surface density for the GMCs in M83. The dashed line indicates the following relation,

$$\sigma_{v,0}^2 = \left(\frac{\sigma_v}{R} \right)^2 = \frac{a_1}{5} \pi G \Sigma_{\text{GMC}}, \quad (9)$$

which is equivalent to $M_{\text{vir}} = M_{\text{GMC}}$ ($\alpha_{\text{virial}} = 1$, i.e., virial equilibrium) if the assumed CO-to- H_2 conversion factor is correct. As a further reference, the dotted line in each plot corresponds to the relation $\alpha_{\text{virial}} = 2$, which is expected for the case of simple gravitational collapse (Ballesteros-Paredes et al. 2011; see also Larson 1981).

Plotting the all samples together (figure 11a), we see that the linewidth–size relation coefficient does depend on the gas sur-

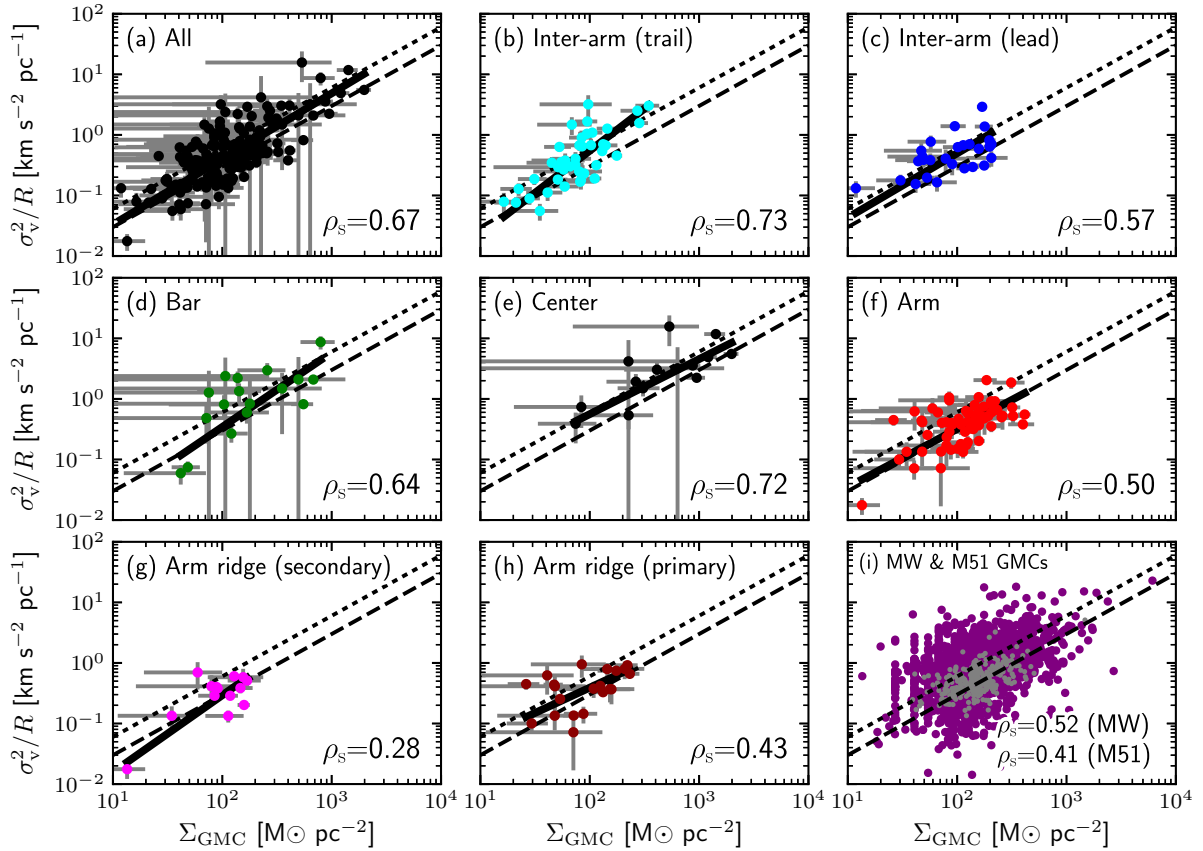


Fig. 11. Same as figure 9, but for the square of the linewidth–size relationship coefficient ($\sigma_{v,0}^2 = \sigma_v^2/R$) as a function of the mean surface density for the GMCs in M83. In each plot, dashed and dotted lines indicate the line for $\alpha_{\text{virial}} = 1$ and $\alpha_{\text{virial}} = 2$.

face density with a modest sign of correlation ($\rho_s \sim 0.67$), and data points are clustered around $\alpha_{\text{virial}} = 1$. Divided into sub-regions, correlation coefficients become lower in some regions, but this seems simply due to the reduced dynamic range of the gas surface density. The lower correlation coefficient obtained for the $\sigma_{v,0} - \Sigma_{\text{GMC}}$ relation compared to the $M_{\text{vir}} - M_{\text{GMC}}$ relation is expected because the former coefficient is derived from the latter by dividing both sides by R^2 and associated constant factors that make the dynamic range of the $\sigma_{v,0} - \Sigma_{\text{GMC}}$ relation smaller.

Galactic GMCs from Solomon et al. (1987) are also clustered around the line $\alpha_{\text{virial}} = 1$ (figure 11i), although ρ_s is low (~ 0.52). The lower correlation coefficient for the MW GMCs would also be due to the limited variation in Σ_{GMC} sampled by the survey of Solomon et al. (1987).

Comparing figures 11(a) and 11(i), it is apparent that the GMCs in M83 cover a wider range of Σ_{GMC} than the samples from Solomon et al. (1987). Therefore, we conclude that the dependence of the linewidth–size coefficient on the surface density at least partly explains why the linewidth–size relation for the GMCs in M83 exhibits weak correlation. The limited dy-

namic range of the size parameter should also play a role. It is notable that Hughes et al. (2013) also observed a weak correlation for the linewidth–size relation in extragalactic GMCs with a nominal procedure of cloud decomposition which tends to identify structures close to a resolution limit. However, with an alternative decomposition procedure that tends to achieve uniform surface density threshold, they obtained a stronger correlation. The stronger correlation obtained with the uniform surface density threshold is in agreement with the fact that $\sigma_{v,0}$ scales as Σ_{GMC} .

4.7 Mass spectrum of GMCs

The mass spectrum of GMCs is known to follow a power-law relation, $dN/dM \propto M^\gamma$. In the inner disk of the MW, the index γ is claimed to be approximately -1.5 by several studies (Solomon et al. 1987; Williams & McKee 1997; Rosolowsky 2005). On the other hand, in the outer disk of the MW, the slope of the GMC mass spectrum is suggested to be steeper compared to the inner disk with γ being smaller than -1.5 (Heyer et al. 2001; Rosolowsky 2005). This difference of γ found be-

tween the inner and outer parts of MW may imply that the mass spectrum of GMCs is not uniform and could vary over different environments. Indeed, nonuniform values of γ are reported by extragalactic studies: citing some examples, in M33, LMC, M51, NGC 300, NGC 4526, and NGC 1068, γ is found to be -2.0 ± 0.2 (Rosolowsky et al. 2007; also -2.0 ± 0.1 by Gratier et al. 2012), -1.75 ± 0.06 (Fukui et al. 2008; although > -2 by Wong et al. 2011), -2.29 ± 0.09 (Colombo et al. 2014), -2.7 ± 0.5 (Faesi et al. 2014), -2.39 ± 0.03 (Utomo et al. 2015), and -1.25 ± 0.07 (Tosaki et al. 2017), respectively. In addition to these galaxy-to-galaxy variations in γ , some of these extragalactic studies also reported regional variations in γ within a galaxy (Rosolowsky et al. 2007; Gratier et al. 2012; Colombo et al. 2014; Utomo et al. 2015).

Another important characteristic of GMC mass spectra is that although most of them could be fitted with a power-law relation at certain mass ranges, some of them are underpopulated at higher masses (e.g., Fukui et al. 2008). To take the deviation from the power-law relation at higher masses into account, it is a common practice to express the mass spectrum with a truncated power law, which is written as follows in integral form (Williams & McKee 1997):

$$N(> M) = -\frac{N_u}{\gamma + 1} \left[\left(\frac{M}{M_u} \right)^{(\gamma+1)} - 1 \right], \quad (10)$$

where M_u is the upper cutoff mass of GMCs. For Galactic GMCs in the inner MW, Williams & McKee (1997) fitted the mass spectrum with this equation and found $\gamma = -1.6$, $M_u = 6 \times 10^6 M_\odot$, and $N_u = 63$, respectively. The total cloud mass integrated over a mass spectrum within the range from the lowest cloud mass M_l to the highest cloud mass M_u is given as

$$M_{\text{total}}(\geq M_l) = \frac{N_u M_u}{\gamma + 2} \left[1 - \left(\frac{M_l}{M_u} \right)^{(\gamma+2)} \right]. \quad (11)$$

If γ is larger than -2 , then massive clouds account for a large proportion of the total cloud mass, and the total cloud mass can be approximately given as $\frac{N_u M_u}{\gamma+2}$. Substituting the parameters for the inner MW quoted above, the total gas mass in the inner MW could be estimated as $\sim 1 \times 10^9 M_\odot$ (Williams & McKee 1997), which is in agreement with other estimates (Heyer & Dame 2015).

The shapes of GMC mass spectra are considered to reflect the properties of the environments from where the GMCs are sampled. In a region where formation of massive GMCs is enhanced, either by collisional agglomeration of preexisting smaller clouds or by the roles of instabilities, the slope of GMC mass spectra would be shallower (e.g., Dobbs 2008). On the other hand, destructive processes such as stellar feedback (Wilson & Scoville 1990) and large-scale shear motion (e.g., Meidt et al. 2015) work to decrease the number of massive GMCs and thus steepen the slope of mass spectra. The variation in γ observed could be due to the environmental variation

in the balance between the formation and destruction processes of GMCs (Inutsuka et al. 2015; Kobayashi et al. 2017).

In this subsection, we will derive the mass spectra of the identified GMCs in M83 and fit them with the truncated power law. The slopes of the fitted mass spectra, γ , will be compared with other extra-galactic studies.

Figure 12 shows the cumulative mass function of the GMCs in M83, for all samples (a) and for each subregion (b-h). The ordinates of the plots are normalized by the area of each region from which GMCs are sampled. Although the mass detection limit is expected to be approximately $2.3 \times 10^5 M_\odot$ in uncrowded regions (§4.1), the minimum masses of the sampled GMCs in the bar and center are approximately $10^6 M_\odot$. On the other hand, in regions other than the bar and center, smaller GMCs with masses down to a few multiples of $10^5 M_\odot$ are sampled, in agreement with the expected detection limit. The elevated detection limits in the bar and center are most likely due to the high background surface density of molecular gas in those regions. As can be seen in figure 2(a), the CO intensity in the bar and center is mostly over the contour line of 48 K km s^{-1} , which corresponds to the molecular gas surface density of $\sim 200 M_\odot \text{ pc}^{-2}$ with the same assumptions made in §3.1. Therefore, GMCs in the bar and center regions are surrounded by 'ambient' gas with a high surface density, comparable to the typical values of Galactic GMCs (Solomon et al. 1987). Only clouds with significant over-densities above the background level of $\sim 200 M_\odot \text{ pc}^{-2}$ can be identified as GMCs. On the other hand, if there is a cloud with a mass of $10^6 M_\odot$ and with a size similar to the spatial distribution (FWHM of $\sim 46 \text{ pc}$), then the average surface density of cloud is $\sim 420 M_\odot \text{ pc}^{-2}$. As this value is only a factor of 2 higher than the background, it is natural that clouds smaller than $10^6 M_\odot$ are not detected in the bar and center regions.

We fitted the cumulative mass function for each region with equation (10), using the GMC samples with a mass between $10^6 M_\odot$ and $3 \times 10^7 M_\odot$. The lower end corresponds to the approximate minimum GMC mass in the bar and the center. The higher end is taken to exclude four clouds with cloud masses of $3.0, 3.4, 4.0,$ and $4.4 \times 10^7 M_\odot$ because their masses are larger than those of other clouds by more than 0.3 dexes and appear as outliers on figure 12(a).

A bootstrap method with 100 draws was used to estimate the confidence interval of the fitted parameters by taking the uncertainties of each GMC mass. A draw for the bootstrap estimation is made by adding random mass noise to each GMC and fitting equation (10) to the cumulative mass function obtained from the data with noise added. The mass noise is derived by assuming a Gaussian distribution with a standard deviation equivalent to the mass uncertainty derived for each GMC. The most likely value and the confidence interval for each parameter were obtained by taking the median and the median absolute deviation

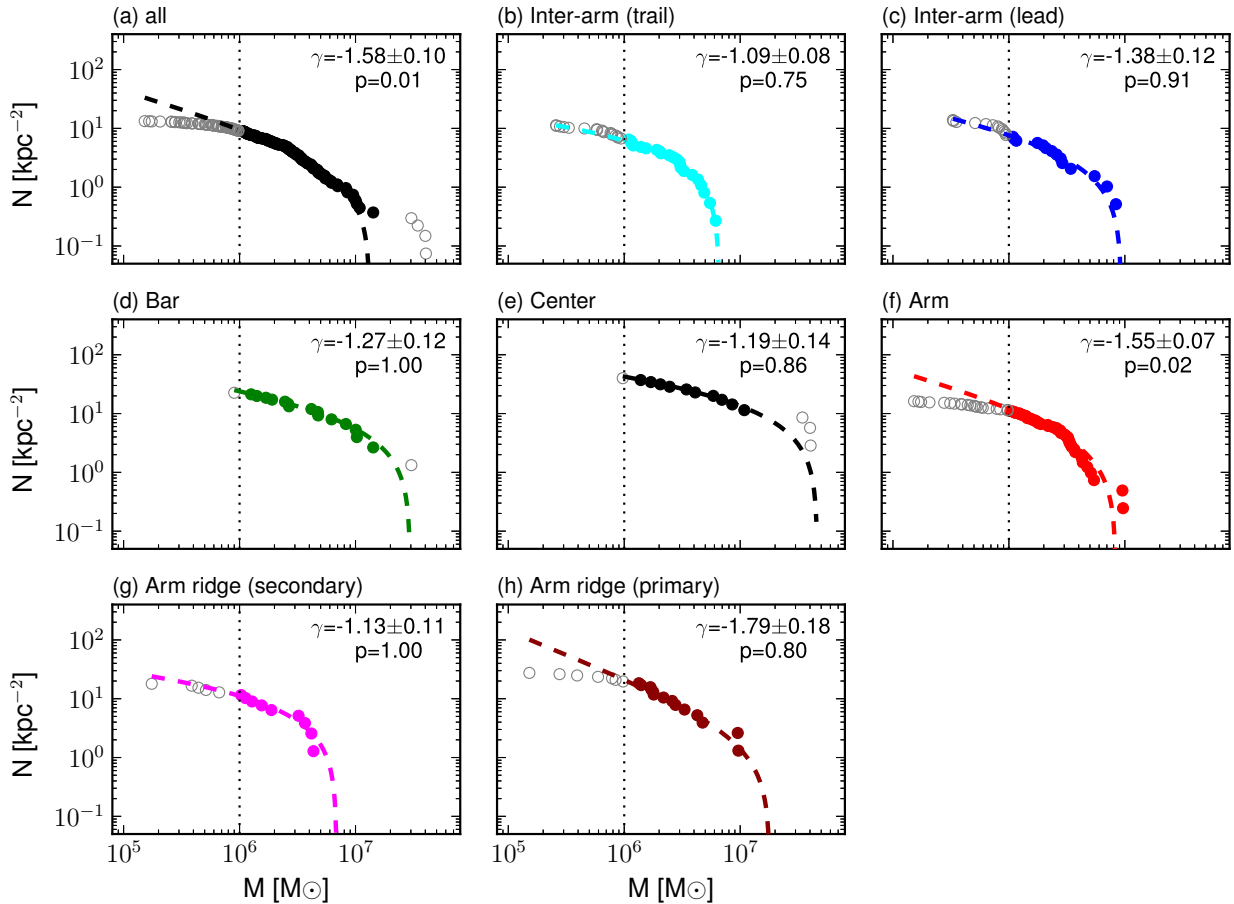


Fig. 12. (a) Cumulative mass function for all of the GMC samples in M83. (b-h) Same as (a), but for the GMCs in each subregion defined in figure 6 (b-h). In each plot, filled and open circles indicate the GMCs that are used and not used for fitting the spectra with equation (10), respectively and the dashed line indicates the fitted function. The dotted vertical line indicates the lower mass limit, $10^6 M_{\odot}$, for the fitting of mass spectra. GMCs with masses below this limit were not used for the fitting. The slope of the fitted mass spectrum, γ , and the p -value for KS test are noted at the top right corner of each plot.

(MAD) of 100 bootstrap realizations for each parameter. After obtaining the most likely values for each parameter, the two-sided Kolmogorov–Smirnov (KS) test was performed to evaluate the goodness of fit. For the KS test, GMCs outside of the fitting range were also included. The resultant fitting parameters along with the p -value for the KS test are summarized in table 3. In addition, table 3 also lists the total cloud mass integrated over the fitted mass spectrum obtained using equation (11) with an M_1 of $10^3 M_{\odot}$ and the sum of the GMC mass for each region.

The fitted mass spectrum for all samples (figure 12a) has a slope of $\sim -1.6 \pm 0.1$, which is in agreement with the value found in the inner disk of the galaxy ($\gamma = -1.6$; Williams & McKee 1997). The KS test reported a low p -value of ~ 0.01 . This is mostly due to the disagreement between the fitted function and the actual data below $10^6 M_{\odot}$, which we suspect to be caused by the elevated detection limit in crowded areas.

Divided into subregions, the slopes of the mass spectrum

show a modest regional variation that ranges between -1.1 and -1.8 . The slope in the arm region (~ -1.6) is steeper than both of the inter-arm subregions (~ -1.1 and ~ -1.4). The two arm ridges located inside the arm also exhibit different slopes from each other. The primary arm ridge has the steepest slope among all of the subregions (~ -1.8). On the other hand, the slope for the secondary arm is ~ -1.2 and is similar to that in the inter-arm regions.

All of the slopes found here are greater than -2 , which implies that massive GMCs dominate a significant fraction of the total cloud mass, as in the MW. With a mass spectrum having a shallow slope, the contribution of smaller clouds is expected to be less important. This point can be confirmed from the closeness between the total mass integrated over the fitted mass spectrum and the summation of the identified GMC mass in regions with shallow γ , such as the inter-arm, bar, and center regions (7th and 8th columns in Table 3).

Table 3. Parameters of the GMC mass distribution

Name	Area ⁽¹⁾ (kpc ⁻²)	γ ⁽²⁾	N_u ⁽³⁾	M_u ⁽⁴⁾ ($10^6 M_\odot$)	p -value ⁽⁵⁾	$M_{\text{cloud, total}}$ ⁽⁶⁾ ($10^7 M_\odot$)	ΣM_{GMC} ⁽⁷⁾ ($10^7 M_\odot$)
all	13.5	-1.58 ± 0.10	21.1 ± 6.3	13.3 ± 2.1	0.01	65.2	56.0
Inter-arm (trail)	3.7	-1.09 ± 0.08	11.4 ± 1.0	6.6 ± 0.3	0.75	8.3	7.6
Inter-arm (lead)	1.9	-1.38 ± 0.12	4.2 ± 0.7	9.3 ± 0.5	0.91	6.3	5.3
Arm	4.1	-1.55 ± 0.07	11.9 ± 1.4	8.4 ± 0.3	0.02	21.6	13.8
Arm ridge (secondary)	0.8	-1.13 ± 0.11	3.9 ± 0.6	6.9 ± 0.6	1.00	3.1	2.4
Arm ridge (primary)	0.8	-1.79 ± 0.18	1.4 ± 1.0	18.0 ± 5.6	0.80	10.9	5.3
Bar	0.8	-1.27 ± 0.12	3.2 ± 1.2	29.7 ± 8.1	1.00	13.0	10.8
Center	0.4	-1.19 ± 0.14	2.5 ± 1.2	46.3 ± 20.7	0.86	14.4	16.3

⁽¹⁾ Area of the region. ⁽²⁻⁴⁾ Parameters of the fitted truncated power-law function. ⁽⁵⁾ The p -value of the KS test. ⁽⁶⁾ The total cloud mass obtained by integrating the fitted mass spectrum within the range $10^3 M_\odot$ to M_u . ⁽⁷⁾ The sum of the GMC masses within the region.

4.7.1 Comparison with other extragalactic measurements of mass spectra

In general, a galaxy-to-galaxy comparison of GMC mass spectra has to be made with great care because differences in the observational setup and in the cloud identification algorithm affect the observed shapes of mass spectra (e.g., Wong et al. 2011). A cloud identified as a single entity with a particular spatial resolution could be divided into several smaller clouds if a finer spatial resolution is utilized. The sensitivity limit also affects the shape of the GMC mass spectrum because if a physical upper limit of the GMC mass exists, the slope of the mass spectrum steepens at a higher mass and thus with a higher mass limit, the observed slope tends to be steeper (e.g., Fukui et al. 2008). For example, while the index γ is found to be ~ -1.75 in LMC with a resolution of 50 pc (Fukui et al. 2008), with a finer spatial solution, Wong et al. (2011) reported a slope of $\gamma \leq -2$.

Despite the difficulty of galaxy-to-galaxy comparison of GMC mass spectra, or more precisely work-to-work comparison, several studies agreed in pointing out that the slope of GMC mass spectra tends to steepen when the galactocentric radius within a galaxy increases (e.g., Rosolowsky et al. 2007; Gratier et al. 2012; Colombo et al. 2014). In general, the fraction of molecular gas is lower in the outer part of a galactic disk compared to the inner disk. Thus, the steeper slope in the outer part could be interpreted as a consequence of the difficulty in building massive GMCs in regions where the amount of molecular gas is lower (Dobbs 2008).

A few galaxies have been investigated for environmental variation in GMC mass spectra with a spatial resolution comparable to the one used here (~ 46 pc). For example, two independent studies reported the radial variation of the index in M33, which changes from $\gamma > -2$ in the inner part, which is within a galactocentric radius of 2.2 kpc, to $\gamma < -2$ in the outer part (-1.8 vs -2.1 in Rosolowsky et al. 2007, -1.6 vs -2.3 in Gratier et al. 2012). The variation in γ apparently correlates with the radial variation in the molecular gas fraction in M33, because the fraction declines from 60% to 20% from the center to the outer disk (e.g., Rosolowsky et al. 2007). Another example is

the environmental variation in GMC mass spectra observed in M51 (Colombo et al. 2014). Within a galactocentric radius of approximately 1.2 kpc ($\sim 30''$) in M51, γ is reported to be -1.3 – -1.6 (regions labeled as the nuclear bar and molecular ring). On the other hand, outside of 1.2 kpc, the reported values of γ range between -1.8 and -2.6 . Therefore, M51 also exhibits a decreasing trend in γ with increasing galactocentric radius. As in M33, the decline in γ is possibly correlated with the radial variation in the molecular gas fraction because the molecular gas fraction within 1.2 kpc is 90% or higher, while outside of 1.2 kpc, it slightly declines to 70%–80% (read from the map in Koda et al. 2009).

The values of γ found in M83 here range between -1.1 and -1.8 , and are shallower than most values found in M33 and M51. The target regions studied here in M83, which are located within a galactocentric radius of 2.6 kpc, are predominantly molecular (§3.1). Therefore, the shallower slopes found here seem to agree with a tendency for the slopes of GMC mass spectra to be shallower in the molecular-dominated part of the galactic disks. We also note that from the examples cited above, similarly shallow slopes are reported only in the central ~ 1.2 kpc of M51 (-1.3 and -1.6 in Colombo et al. 2014).

4.7.2 Possible interpretation of the variation in the mass spectrum slope

Inutsuka et al. (2015) and Kobayashi et al. (2017) pointed out that if the continuity equation of molecular clouds in mass space is assumed, the slope of the mass spectrum, γ , could be described as

$$\gamma = -(1 + T_{\text{f}}/T_{\text{d}}), \quad (12)$$

where T_{f} and T_{d} are the time scales for the formation and destruction processes of molecular clouds, respectively. Although the formation and destruction timescales are not well constrained at this moment, the essence of equation 12, which is the dependence of γ on the formation and destructive processes, appears qualitatively in agreement with suggestions made by previous studies. For example, Dobbs (2008) suggested that

in regions where formation of massive GMCs is enhanced, the mass spectrum slope becomes shallower. On the other hand, Wilson & Scoville 1990 suggested that in regions where stellar feedback are effective enough to depopulate massive GMCs, the slope becomes shallower (Wilson & Scoville 1990).

As we have seen in the previous subsection, the slopes of the GMC mass spectra obtained here range from -1.1 to -1.8, which are rather shallow compared to the values obtained in other studies that have investigated the regional variation in GMC mass spectra within a galaxy (Rosolowsky et al. 2007; Gratier et al. 2012; Colombo et al. 2014). As the gas disk within the observed region is already predominantly molecular, GMCs do not have to be formed from atomic gas but instead are formed directly from molecular gas (Dobbs 2008). In light of the idea that the balance between the formation and destruction timescales of GMCs determines the shape of the GMC mass spectrum (Inutsuka et al. 2015; Kobayashi et al. 2017; also Wilson & Scoville 1990), the shallow slopes found here in M83 might be a reflection of effective formation of massive GMCs in the molecular-dominated gas disk with a short T_f .

We also speculate that the steeper slope found in the primary arm ridge (-1.8) compared to the other regions in M83 studied here is a result of the enhanced influence of stellar feedback, which effectively shortens T_d . We will see later in §6.2 that in the primary arm ridge, GMCs exhibit an elevated SFE and many of them appear to be disrupted by stellar feedback. If the destructive role of stellar feedback is more efficient in the primary arm ridge compared to other regions, then T_d would be effectively shorter and thus the slope of the mass spectrum steeper.

5 Star formation in GMCs

As referred to in the introduction, GMC scale examination of the SFE is important to address how star formation in GMCs and galaxies is regulated to achieve Gyr-long depletion time. In this section, we examine the SFR of the GMCs in M83 presented in the previous section. We will derive the SFR for individual H II regions (§5.1) and then cross-match H II regions with the GMCs (§5.2). Using the cross-matched data sets, we will examine their SFE (§5.3, §5.4, and §5.5).

5.1 Derivation of SFR for individual H II regions

5.1.1 Derivation of $H\alpha$ luminosity

The catalog of the H II region presented in §3 is used as a starting point for the derivation of the SFR. As stated in §3, the $H\alpha$ luminosity for each H II region has been corrected for the contamination of [N II] lines and foreground extinction using the correction factors presented by Meurer et al. (2006). We further corrected for the internal extinction of the H II regions by

utilizing the image of the $Pa\beta$ line emission presented in §3. A median filter with a size of $\sim 8''$ was applied to the $Pa\beta$ image to remove the background emission and the residual of continuum subtraction. Subsequently, the filtered image was smoothed to align the resolution with the $H\alpha$ image, and the $Pa\beta$ flux value was calculated by using the spatial mask defined by HIIphot (Thilker et al. 2000).

The extinction curve of Cardelli et al. (1989) and the intrinsic ratio of $I_{H\alpha}/I_{Pa\beta} = 17.1$ (Dopita & Sutherland 2003) were assumed in deriving $A_{H\alpha}$ from the measured $Pa\beta$ and $H\alpha$ flux for each H II region. For the H II regions that are within the FOV of the $Pa\beta$, the median and MAD of the derived $A_{H\alpha}$ are found to be 1.9 mag and 1.1 mag, respectively. For the H II regions that are outside the FOV of the $Pa\beta$ image, we assign $A_{H\alpha}=1.9$ mag to them with an error bar of 1.1 mag.

5.1.2 Derivation of SFR

To derive SFR from the $H\alpha$ luminosity, we use the SFR calibration provided by Calzetti et al. (2007):

$$SFR (M_{\odot} \text{ yr}^{-1}) = 5.3 \times 10^{-42} L(H\alpha) (erg \text{ s}^{-1}). \quad (13)$$

We note that this calibration factor is calculated using the Starburst99 model (Leitherer et al. 1999) by assuming a constant SFR with the Starburst99 default stellar initial mass function (IMF), which resembles the IMF of Kroupa (2001). The assumption of a constant SFR requires steady state balance between the number of ionizing stars that are forming and dying: at least ~ 6 Myr of continuous star formation at a constant rate is needed to achieve this, and thus it might be unrealistic to expect this assumption to hold for individual H II regions. In fact, by modeling the observed $H\alpha$ and UV luminosities for H II regions in NGC 300, Faesi et al. (2014) derived calibration factors that produce on average a factor-of-2-higher SFR than the Calzetti et al. (2007) calibration does. As we have not constrained the star formation history of individual H II regions yet, we just adopt the conventional extra-galactic calibration of Calzetti et al. (2007) here but note that the SFR derived here could be underestimated by approximated a factor of 2.

5.2 Cross-matching

To identify host GMCs for H II regions, we cross-match the H II region catalog with the GMC samples presented in §4. As H II regions can drift away from host GMCs and can also expel the surrounding molecular material by stellar feedback, they do not necessarily reside within the densest part of host GMCs. To account for this effect, we adopted ellipses that define effective major and minor radii for GMCs as their boundaries, which are the same as the ones shown in figure 5. If the central position of an H II region is within the boundary of a GMC, then the H II region is judged to be associated with the GMC. Figure 13 shows the spatial relationship between the H II regions and the

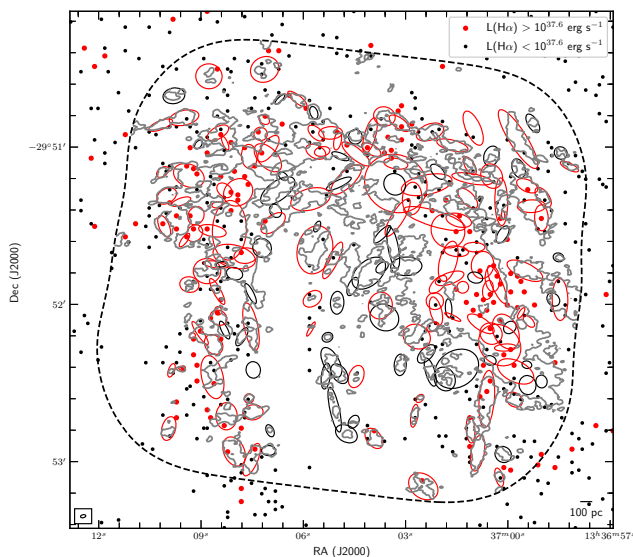


Fig. 13. Distribution of H II regions shown together with the distribution of GMCs overlaid on the integrated CO image with a contour line at 13 K km s^{-1} . Black and red ellipses indicate the position of the GMCs without and with associated H II region(s). The size of the ellipses indicates effective major and minor radii for the GMCs, which are the same as the ones shown in figure 5.

GMCs.

Out of a total of 179 GMCs, 122 GMCs are found to be associated with one or more H II regions. Sixty-six GMCs are associated with a single H II region each, and 56 GMCs are associated with more than one H II region each. If an H II region has a one-to-one relationship with a GMC, then the SFR for the H II region is just directly registered to the GMC. For an H II region that is associated with multiple GMCs, the SFR of the H II region is divided among the associated GMCs, weighted by the cloud mass.

There also exist 57 GMCs that lack associated H II regions. For these GMCs without H II regions, we set an upper limit on the SFR. From the distribution of the uncorrected $\text{H}\alpha$ luminosity, we determined the completeness limit of H II region detection to be approximately $10^{37.1} \text{ erg s}^{-1}$. By adopting the median value for the internal extinction, $A_{\text{H}\alpha}=1.9$, and using equation (13), the completeness limit for the detection of H II regions is translated into the limiting SFR of $3.5 \times 10^{-4} M_{\odot} \text{ yr}^{-1}$. We just take this SFR value as an upper limit for the SFR of GMCs that lack associated H II regions. The assumption involved here is that even some H II regions with an $\text{H}\alpha$ luminosity comparable to $10^{37.1} \text{ erg s}^{-1}$ could fail the H II phot identification and not find a place in the H II region catalog used here, such bright but undetected H II regions are rare, and thus a GMC is associated with at most one of those undetected H II regions. We believe that this is not an overoptimistic assumption because over half

of the H II regions associated with GMCs have a one-to-one relation and as most of the GMCs that lack associated H II regions reside in inter-arm regions, where H II regions are sparse (figure 13). We also note that this upper limit is rather conservative, because approximately one-third of the H II regions have uncorrected $\text{H}\alpha$ luminosity under the adopted completeness limit of $10^{37.1} \text{ erg s}^{-1}$, down to $\sim 10^{36.0} \text{ erg s}^{-1}$.

The upper limit on the SFR adopted here also satisfies the requirement that our method for the SFR derivation requires the presence of at least one massive star so that H II region can be identified. The mean lifetime of ionizing stars averaged over the stellar IMF is $\sim 4 \text{ Myr}$. If stars form with a constant rate of $3.5 \times 10^{-4} M_{\odot} \text{ yr}^{-1}$, which is the adopted upper limit on the SFR, for 4 Myr, $\sim 1400 M_{\odot}$ of stellar mass is produced. On the other hand, $\sim 1000 M_{\odot}$ of stellar mass is enough to sample the stellar IMF in the sense that at least one O star is produced (Calzetti et al. 2010; Koda et al. 2012).

5.3 GMC scale view of SFE

Figure 14 shows the relationship between the SFR and the molecular gas mass for the GMCs in M83. GMCs that lack associated H II regions are indicated with an upper limit on the SFR.

To compare with the GMCs in M83, we incorporated some literature values into the plot. Lada et al. (2010) estimated the SFR and the gas mass for nearby star-forming clouds that are located closer than 500 pc from the Sun, based on the number of young stellar objects (YSOs) and the K -band extinction, respectively. Cloud samples in Lada et al. (2010) with mass greater than $5 \times 10^3 M_{\odot}$ are included in the plot. In addition, we have included G216-2.5, a Galactic cloud considered as an archetype for a low-activity cloud (also known as Maddalena's cloud; Maddalena & Thaddeus 1985). Lee et al. (1996) and Megeath et al. (2009) detected a few YSOs around and within this cloud, respectively. On the basis of their YSO counts, Imara (2015) estimated the SFR of this cloud to be $\sim 33 M_{\odot} \text{ Myr}^{-1}$. The ^{12}CO luminosity of G216-2.5 is $6.1 \times 10^4 \text{ K km s}^{-1}$ (Lee et al. 1994). Thus, using equation (2), we estimated the cloud mass to be $2.7 \times 10^5 M_{\odot}$. We note that there exist several other estimations for this cloud. Imara (2015) estimated the mass to be $1.2 \times 10^5 M_{\odot}$ on the basis of the far-infrared luminosity, which is close to another mass estimate made by Lee et al. (1994) on the basis of the ^{13}CO luminosity with an assumption of local thermodynamic equilibrium ($1.1 \times 10^5 M_{\odot}$). In addition to the Galactic clouds, H II regions in NGC 300, which are detected in CO with 250 pc resolution (Faesi et al. 2014), are also included in the plot.

A comparison of the SFR between the the GMCs in M83 and the Galactic samples quoted here has to be treated with care. The SFR for GMCs in M83 is derived by tracing the

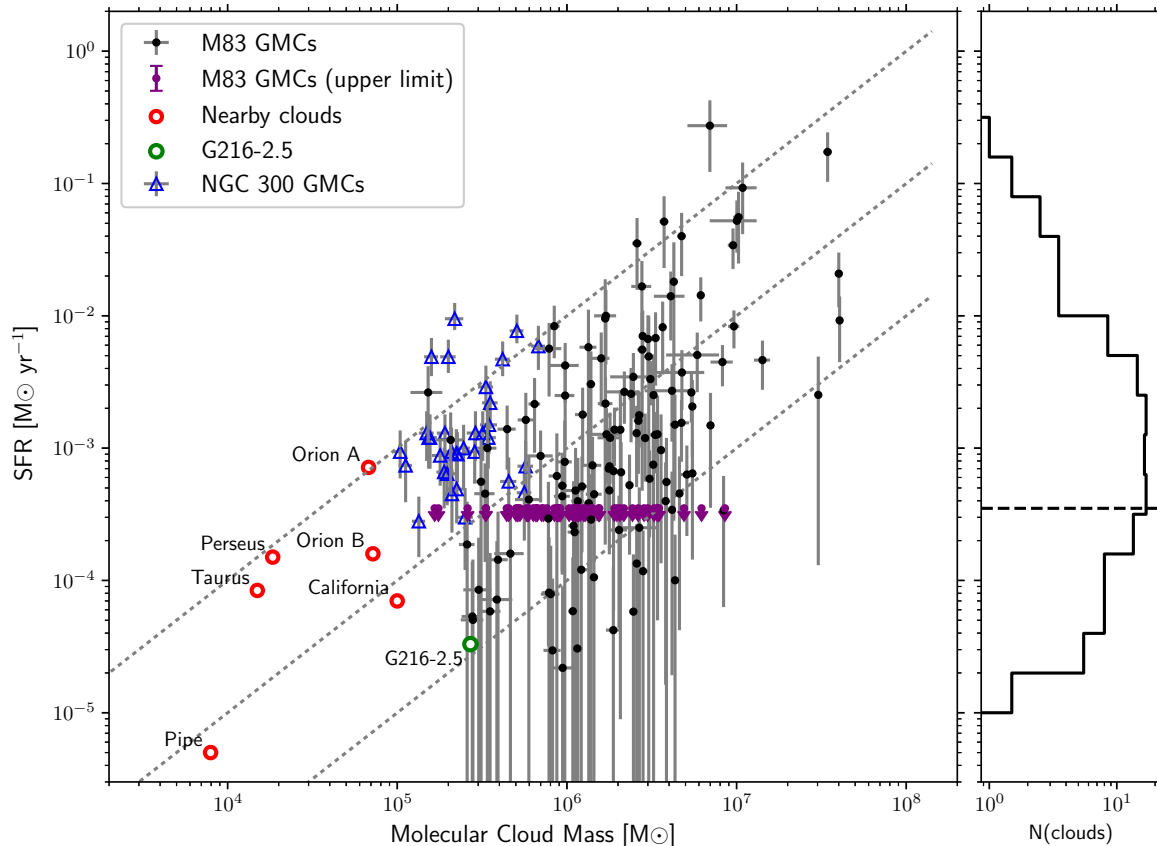


Fig. 14. (Left) Star formation rate (SFR) to cloud mass relation for the GMCs in M83. Black dots with error bars represent the GMCs with an associated H II region. The GMCs without an associated H II region are indicated with the upper limit on SFR (purple). Red open circles indicate nearby star-forming regions taken from Lada et al. (2010). The green circle indicates the data for G216-2.5. Blue triangles indicate H II regions in NGC 300 that are detected in CO with ~ 250 pc resolution (Faesi et al. 2014). Dotted lines indicate lines of constant star formation efficiency (SFE) for 0.1, 1, and 10 Gyr^{-1} , respectively. (Right) Histogram of the SFR assigned to individual GMCs in M83. The dashed horizontal line indicates the limit on SFR assigned to GMCs that are not associated with H II regions.

$\text{H}\alpha$ emission from H II regions, which are almost solely powered by massive stars. As the nominal lifetime of massive stars is ~ 4 Myr, the SFR derived from the $\text{H}\alpha$ emission is a time-averaged value with a window size of ~ 4 Myr. On the other hand, the SFR for Galactic GMCs is derived with a shorter window size because it is based on the number counts of YSOs, which formed within the last 2 ± 1 Myr (e.g., Evans et al. 2009). The YSO counting method has a further advantage that it samples much smaller stars compared to the $\text{H}\alpha$ method. Thus it is less affected by stochastic samplings of the stellar IMF. From the comparison of different SFR calibration methods applied to Galactic clouds, Chomiuk & Povich (2011) concluded that the SFR derived with YSO counting methods are approximately a factor of 2 to 3 higher than either of the SFR derived from the $24\mu\text{m}$ flux or the Lyman continuum production rate.

Despite the uncertainty about the relative consistency between the different SFR calibration methods, the GMCs in M83 share similar characteristics as the Galactic clouds in regard to

SFE, defined as the ratio between the SFR and the cloud mass. The data points for the GMCs in M83 fall in the SFE range between 0.1 and 10 Gyr^{-1} , indicating that the peak-to-peak SFE variation is approximately two orders of magnitude. This scatter is comparable to the values found in Galactic GMCs (Mooney & Solomon 1988; Murray 2011; Lee et al. 2016). Specifically, the median value of the SFE is $\sim 0.5 \text{Gyr}^{-1}$ for the M83 GMC samples, and the scatter is 0.52 dex in MAD. We note that the range of SFEs observed in the M83 GMCs is comparable to that found in the Galactic cloud samples plotted in figure 14, which places G216-2.5 and Orion A at the both ends.

5.4 Radially averaged SFR to mass relation for GMCs

In this subsection, we inspect the relation between the surface density of the SFR and the GMC mass on a radial average basis. First, the SFR surface density per unit area, Σ_{SFR} , of each GMC

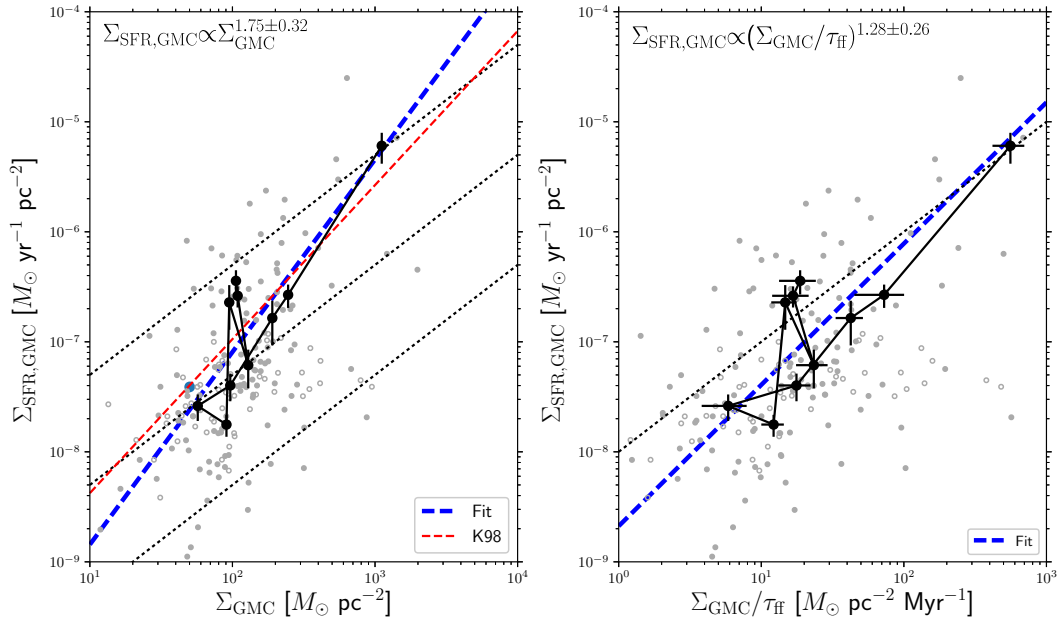


Fig. 15. (Left) Relation between SFR per unit area and gas surface density for GMCs. Gray filled and open circles indicate the data for individual GMCs with and without associated H II regions, respectively. Black circles with error bars indicate the radially averaged data, calculated with radial bins specified with galactocentric radius ranges of 0–12, 12–24, 24–36, ..., and 108–120 arcseconds, respectively. Neighboring radial data points are connected to each other with solid lines. In each plot, the data point with the highest surface mass density indicates the innermost radial bin. The blue heavy dashed line indicates the fitted function. The red dashed line indicates the relation given by Kennicutt (1998) but scaled by a factor of 0.67 to account for the difference of the assumed stellar IMF. Dotted lines are for constant depletion times of 0.2, 2, and 20 Gyr, respectively. (Right) Same as the left one, but for SFR per unit area and gas surface density divided by the free-fall time for GMCs. The dotted line is for a constant SFE_{ff} of 0.01.

is derived by dividing the SFR by the effective area of GMC, πR_{eff}^2 . Next, radial bins with a width of $12''$ (~ 264 pc) are generated, and the radially averaged values of Σ_{SFR} and Σ_{GMC} are derived. Figure 15 (left) plots the relation between Σ_{SFR} and Σ_{GMC} . The solid line in the plot indicates the radially averaged values of Σ_{SFR} and Σ_{GMC} . In calculating the radial average, the SFR for the GMCs without associated H II regions are calculated with upper limits on the SFR. Therefore, the radially averaged values in this plot have to be treated as upper limits.

A least-square fitting is made to the radially averaged data points by minimizing the effective variance (Orear 1982). The fitted slope is 1.71 ± 0.31 , which is well above unity. This super-linear relation does not contradict the well-quoted non-linear index of 1.4 ± 0.15 (Kennicutt 1998) obtained by fitting data of nearby galaxies. For reference, the relation of Kennicutt (1998) is overplotted with a modification of the coefficient to adjust for the difference in the assumed stellar IMF. The radially averaged data points are within a factor of three variations from the relation of Kennicutt (1998) and appear to be in reasonable agreement with it.

Next, we divide the quantity on the abscissa, Σ_{GMC} , by the free-fall time of the GMC. If the SFR and SFE are characterized by a constant or a nearly constant SFE_{ff} , then the observed data points should exhibit a linear relation. Figure 15 (right) shows the relation between the radially averaged Σ_{SFR} and $\Sigma_{\text{GMC}}/\tau_{\text{ff}}$.

We also fit a proportional relationship, $\Sigma_{\text{SFR}} \propto \Sigma_{\text{GMC}}/\tau_{\text{ff}}$, to the radial data points to estimate a proportionality coefficient, which is SFE_{ff} . The resultant value for SFE_{ff} is $5.8_{-1.4}^{+1.8} \times 10^{-3}$ and is not far from the well quoted value of 0.01 (e.g., Krumholz et al. 2012).

The results obtained with radially averaged data points are not so sensitive to the way H II regions are associated with GMCs (§5.2). If the threshold radius for associating H II regions with GMCs is changed, it is possible that an H II region associated with a GMC with a particular threshold will be assigned to other neighboring GMC with a different threshold. However, as Σ_{SFR} and Σ_{GMC} are averaged within radial bins, the shift of SFR from a GMC to another GMC is not expected to make a severe impact. Indeed, if the association radius is increased and decreased by 20% (by 44% in terms of the area), the index changes are 1.63 ± 0.30 and 1.86 ± 0.32 for the $\Sigma_{\text{SFR}}-\Sigma_{\text{GMC}}$ relation and 1.33 ± 0.26 and 1.20 ± 0.25 for the $\Sigma_{\text{SFR}}-\Sigma_{\text{GMC}}/\tau_{\text{ff}}$: these values are consistent with each other.

Another source of uncertainty is the different detection limits of GMCs in different environments (§4.7). In figure 15 (left), the single data point with the highest Σ_{GMC} has a strong influence in determining the index of the fitted function, and this also applies for figure 15 (right). The area of the radial bin for that point overlaps with the central region in which the minimum of the detected GMC masses is a factor of few higher than in un-

crowded regions, such as the inter-arm regions. Thus, one might suspect the lack of smaller clouds in the central region may have a significant impact on the fitted parameters. However, GMC mass spectra investigated in §4.7 exhibited slopes shallower than $\gamma < -2$. In particular, the slope γ in the central region is quite shallow with $\gamma \sim -1.2$. With the fitted parameters in the central region and using equation (11), clouds with masses between 10^3 and $10^6 M_\odot$ are expected to comprise less than 5% of the total cloud mass above $10^3 M_\odot$. Therefore, it seems reasonable to suppose that the impact of the varying detection GMC limits is not significant.

Thus far, as far as the averaged data points are concerned, or in other words, as seen on a global scale, the star-forming properties of the GMCs in M83 are in agreement with the model that star formation takes place with a nearly constant efficiency per free-fall time. However, from figure 15 (right), the GMC-to-GMC variation in SFE_{ff} appears to be large. We will investigate the environmental dependence of SFE_{ff} in the next subsection (§5.5) and will discuss it in §6.1 and §6.3.

5.5 SFE_{ff} for individual GMCs

Now we proceed to examine SFE_{ff} for individual GMCs. We derive SFE_{ff} for each GMC as

$$SFE_{\text{ff}} = \frac{\text{SFR}}{M_{\text{GMC}}} \tau_{\text{ff}}. \quad (14)$$

Quantities on the right hand side, SFR, M_{GMC} , and τ_{ff} , are taken from the values determined for each GMC.

We must note that accurate determination of SFE_{ff} for individual GMCs is far from trivial because the stochastic sampling effect of the stellar IMF and the uncertainty of the age introduce errors when deriving the SFR. Further, as the SFRs used here are derived from $H\alpha$ luminosities, they are essentially time-averaged values with a window size of approximately 3–4 Myr because the production rate of the Lyman continuum from a stellar cluster quickly decays after the deaths of massive stars (Murray 2011). This duration is close to the time scale for an individual GMC: the free-fall time is approximately 6–10 Myr for GMCs. Feldmann & Gnedin (2011) pointed out that observationally derived SFE_{ff} values for individual clouds have to be treated as ‘apparent’ values, because if a significant fraction of the gas mass is lost during the averaging time imposed by the SFR tracer, the observed value of SFE_{ff} should be biased upward. Despite these uncertainties, we first just review the observed distribution of SFE_{ff} in this subsection. Later in the next section, we will discuss the effects that can contribute to increasing the apparent variation in SFE_{ff} .

Figure 16 shows histograms of the derived SFE_{ff} for the GMCs for each regional mask. In table 4, we list the mass-weighted mean ($\langle SFE_{\text{ff}} \rangle$), median, and MAD of SFE_{ff} for each regional mask. The mass-weighted mean of SFE_{ff} , $\langle SFE_{\text{ff}} \rangle$,

Table 4. Mean, median, and MAD of SFE_{ff}

	$\langle SFE_{\text{ff}} \rangle$ (%)	Median (%)	MAD (dex)
all	0.93	0.30	0.60
Inter-arm (up)	0.44	0.34	0.47
Inter-arm (down)	0.26	0.24	0.41
Arm	1.48	0.40	0.79
... Arm ridge (secondary)	0.36	0.20	0.46
... Arm ridge (primary)	2.68	2.17	0.81
Bar	0.92	0.24	0.78
Center	1.00	0.21	1.16

for all GMC samples is $\sim 9.3 \times 10^{-3}$. This value is close to the value of ~ 0.01 assumed in many theories based on turbulence-regulated star formation (e.g., Krumholz & McKee 2005; Krumholz et al. 2012). By changing the association radius by $\pm 20\%$ as was done in the previous subsection, the mass-weighted mean changes to $0.79\text{--}1.06 \times 10^{-2}$ and is still in agreement with ~ 0.01 . The agreement of the mass-weighted mean of SFE_{ff} with 0.01 appears to reconfirm the fact the models of turbulence regulated star formation have succeeded in describing the global averaged property of star formation.

Although $\langle SFE_{\text{ff}} \rangle$ shows good agreement with the theoretical expectation, we also see a huge scatter in the distribution of SFE_{ff} if all samples are taken together (figure 16a). The observed peak-to-peak variation in SFE_{ff} is approximately three orders of magnitude and is consistent with other studies that also reported huge cloud-to-cloud variations of SFE_{ff} (Murray 2011; Lee et al. 2016). As foreseeable from the large scatter, the median value of SFE_{ff} is lower $\langle SFE_{\text{ff}} \rangle$, and is 3.0×10^{-3} . We note that Leroy et al. (2017) reported similar value of $3\text{--}3.6 \times 10^{-3}$ in M51 using infrared emission as SFR tracer at resolutions of ~ 370 pc and ~ 1100 pc.

In addition, the variation in SFE_{ff} exhibits a strong regional dependence (figure 16b-h). For almost all of the clouds in the inter-arm regions, SFE_{ff} is below the global average of 0.01. Most GMCs in the bar also show SFE_{ff} values below 0.01, although there is one GMC that exceeds $SFE_{\text{ff}}=0.01$. The center and the arm contain several GMCs that exceed $SFE_{\text{ff}}=0.01$. Within the arm, however, the two arm ridges exhibit a clear difference from each other concerning the distribution of SFE_{ff} : GMCs with SFE_{ff} values higher than 0.01 are concentrated in the primary arm ridge, while in the secondary arm ridge, almost all of the GMCs are below $SFE_{\text{ff}}=0.01$.

6 Discussion

6.1 Is there intrinsic environmental variation of the SFE_{ff} ?

In the previous subsection, we find that there are approximately three orders of magnitude peak-to-peak spread in the values

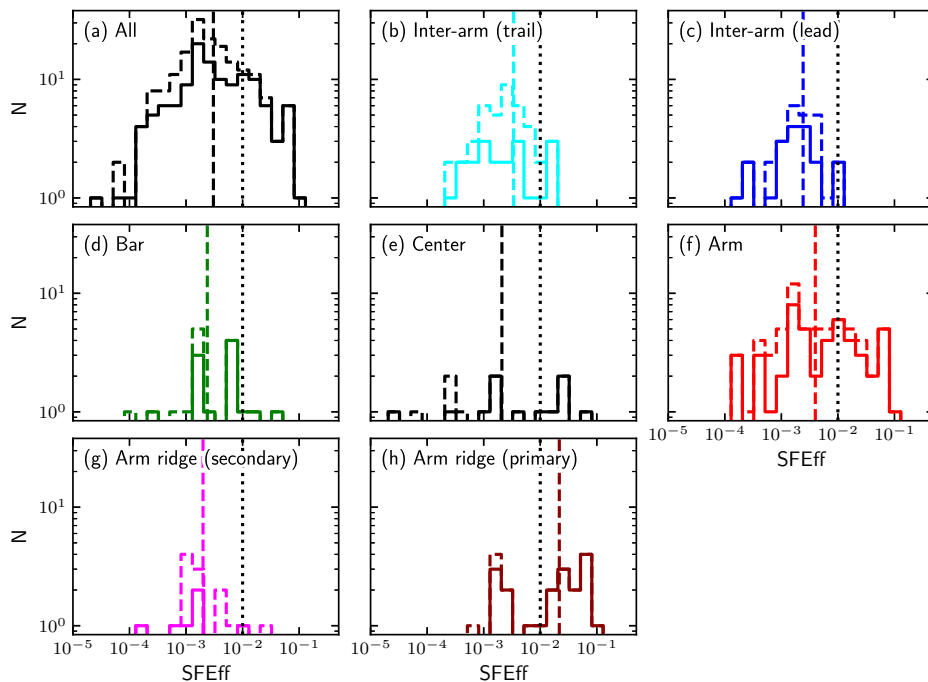


Fig. 16. Histogram of SFE_{ff} plotted for each region. In each plot, the solid histogram shows the number distribution of SFE_{ff} for the GMCs that have associated H II regions. The dashed histogram in each plot includes both GMCs with and without associated H II regions. For the GMCs without associated H II regions, upper limits on SFE_{ff} are used to calculate the dashed histogram. The dotted vertical line indicates an SFE_{ff} of 0.01, which is the mass-weighted mean value for all of the GMCs in M83. The dashed vertical line in each plot indicates the median value of SFE_{ff} for the samples contained in the plot. Note that only in the primary arm ridge is the median SFE_{ff} higher than the global mass-weighted average value of 0.01.

of observationally derived SFE_{ff} . Not only is the scatter of the distribution large, but there are also regional variations in SFE_{ff} . In particular, the two ridges within the arm exhibited a clear difference from each other concerning the distribution of SFE_{ff} . Before discussing the meaning of the regional variation in SFE_{ff} , we first discuss possibilities that the large scatter and regional variations in SFE_{ff} are actually caused by observational effects that produce ‘apparent’ variations in SFE_{ff} even if SFE_{ff} is intrinsically a constant parameter. We consider three mechanisms here: (1) stochastic sampling of the stellar IMF, (2) uncertainty of stellar ages that affects the SFR calibration factor, and (3) mass consumption of GMCs due to stellar feedback.

6.1.1 Sampling effect of the stellar IMF

If a cluster that illuminates an H II region contains a small number of stars, ionizing stars are likely less populated due to the stochastic sampling of the stellar IMF. This sampling effect will lead to an underestimation of the SFR for small H II regions. One might suspect this sampling effect could be responsible for the apparent variation in SFE_{ff} , especially for the GMCs in inter-arm regions that exhibited an SFE_{ff} value that is systematically lower than the global mean of 0.01. However, the variation in SFE_{ff} seen in the previous subsection was revealed with a conservative upper limit on the SFR of $3.5 \times 10^{-4} M_{\odot} \text{ yr}^{-1}$.

If this level of the SFR continues for 3–4 Myr, which is the nominal lifetime of ionizing stars, approximately $1100\text{--}1400 M_{\odot}$ of stellar mass is produced. On the other hand, $\sim 1000 M_{\odot}$ of stellar mass is enough to avoid the severe effect of stochasticity of the stellar IMF sampling: for example, Calzetti et al. (2010) examined the $H\alpha$ luminosity per stellar mass for clusters and indicated that the cluster-to-cluster variation is a factor of 2 for $\sim 1000 M_{\odot}$ clusters. Thus, as long as the sampling effect of the stellar IMF alone is taken into account, the possible amount of the scatter for the apparent value of SFE_{ff} is at most a factor of 2 and is insufficient to explain the observed variation in SFE_{ff} .

6.1.2 Uncertainty of stellar ages

As stated in §5.1.2, the uncertainty of the star formation history for individual H II regions should make the SFR calibration factor, which relates the SFR and $H\alpha$ luminosity, somewhat uncertain. We consider here whether the observed regional variation in SFE_{ff} could be explained by variations in the SFR calibration factor.

If stars in a cluster powering an H II region are formed instantaneously, the production rate of Lyman photons from the cluster decay quickly after 3–4 Myr because of the deaths of massive stars (e.g., Fig. 22 of Scoville et al. 2001; Fig. 1 of Murray 2011). The strong time evolution of the Lyman contin-

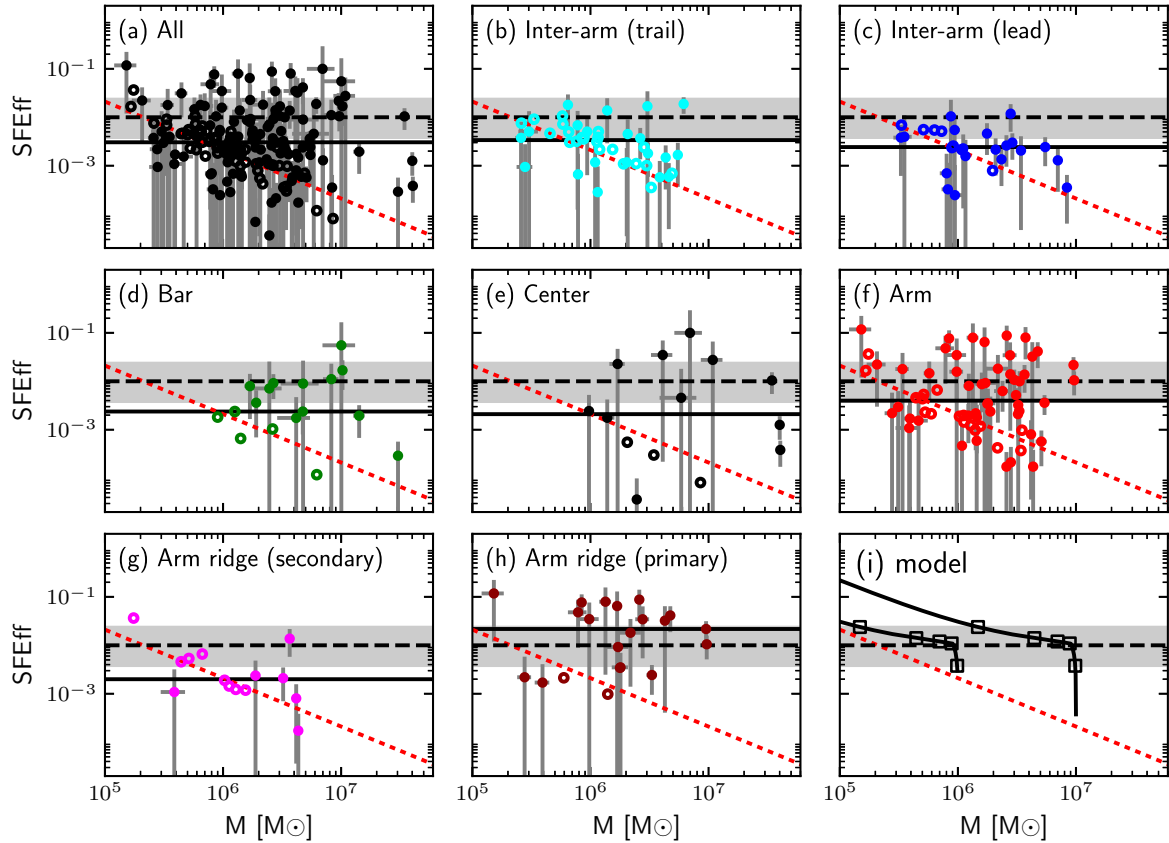


Fig. 17. (a-h) Observationally derived 'apparent' value of SFE_{ff} as a function of cloud mass for the GMCs plotted for each regional mask. The dotted red line in each plot indicates the nominal limit for the detection, obtained by assuming a constant SFR of $3.5 \times 10^{-4} M_{\odot} \text{ yr}^{-1}$ and a free-fall time of $\tau_{ff} = 6.7$ Myr. (i) Curves that show the evolution of SFE_{ff} for model GMCs calculated with the toy model of Feldmann & Gnedin 2011. The left and right curves indicate the evolution of model GMCs with initial masses of 10^6 and $10^7 M_{\odot}$, respectively. The intrinsic value efficiency, $SFE_{ff,i}$, is fixed as 0.01. The feedback parameter is chosen such that the stellar feedback limits the lifetime of model clouds to 20 Myr. Squares indicate the time steps for 10%, 30%, 50%, 70%, and 90% of the lifetime of model GMCs. Gray shaded area in each plot indicates the range of SFE_{ff} covered by model GMCs within 10% and 90% of their lifetimes.

um production rate implies there should be a time evolution of the SFR calibration factor. To see the degree of the time variation of the SFR calibration factor, we here perform a simple calculation using Starburst99. We assume the stellar IMF of Kroupa (2001), solar metallicity, and the burst mode of star formation, which produces all the stars in a cluster at the same time. From the calculated results, we find that the $H\alpha$ luminosity per stellar mass is almost constant for the first 2 Myr, and then starts to decline due to the deaths of the ionizing stars, being about 50%, 20%, and 10% of the initial value at approximately 3.5, 4.5, and 5 Myr, respectively.

The average value of SFE_{ff} in the arm region (~ 0.015) is approximately a factor of 3–5 larger than in the inter-arm regions (~ 0.0046 and ~ 0.0027). As far as the burst mode of star formation in clusters is concerned, the only way to produce this amount of variation in SFE_{ff} by just changing the SFR calibration factor is to assume that the H II regions in the inter-arm are preferentially older than those in the arm regions by a few

Myr. Referring to the values obtained with the Starburst99 calculation, if the H II regions in the arm region are younger than 2 Myr and the ones in the inter-arm regions are older than 4 Myr, it is possible to produce a factor of 3–5 variation in the apparent distribution of SFE_{ff} . However, considering the global galactic dynamics, the dwelling time of GMC in the inter-arm region should be a few to several tens of Myr for the galactocentric radii considered here (figure 17 in Hirota et al. 2014). The dwelling time is much longer than the time for the $H\alpha$ luminosity of an H II region to decay. Thus, the existence of H II regions in the inter-arm regions means that at least some of them are formed in situ. Therefore, it is difficult to consider a process that produces just a few Myr difference in the age distributions of H II regions across the spiral arm and it is unlikely that the observed variation in SFE_{ff} is simply due to the uncertainty of the star formation history.

The conclusion arrived at here will not change even if a cluster was created through several events of star formation that oc-

curred over a few Myr (e.g., Venuti et al. 2018). If a cluster that powers an H II region was formed in a single instantaneous event, then the lifetime of the H II region is approximately 5 Myr, as we have seen above. If a cluster was formed through several events spread over a few Myr, then the lifetime of the H II region is lengthened by a few Myr. However, even if the extra few Myr has to be added to 5 Myr, the lifetime of H II regions is still likely below 10 Myr and well below the dwelling time in the inter-arm region.

6.1.3 Rapid mass consumption of GMCs within the averaging time for the derivation of SFR

The H α emission from an H II region that is used to trace its SFR quickly decays after approximately 4 Myr, because of the deaths of massive stars. Therefore, the SFR derived from the H α luminosity of an H II region is essentially a time-averaged value with an averaging window length of approximately 4 Myr (e.g., Murray 2011). On the other hand, once massive stars are formed inside a GMC, they are considered to be capable of ionizing and disrupting a significant portion of the parental GMC within a timescale of a few tens of Myr (e.g., Whitworth 1979; Williams & McKee 1997), which is comparable with the estimated GMC lifetimes (15–40 Myr; Kawamura et al. 2009; Murray 2011; Miura et al. 2012). The suggested timescale for cloud destruction is only a few times longer than the averaging window length of ~ 4 Myr for the derivation of the SFR. Therefore, a GMC associated with the H II regions could have lost a non-negligible fraction of its mass due to the stellar feedback within the averaging duration. If this is the case, then the SFE_{ff} derived from the observed SFR and cloud mass should be biased upward.

6.1.3.1 Cloud mass evolution model. To investigate the impact of this time evolution effect, we employ a toy model introduced by Feldmann & Gnedin (2011), which solves a differential equation of mass evolution for a GMC:

$$\frac{dM_{\text{GMC}}}{dt} = SFR(t) - \alpha_{\text{fb}} M_*(t), \quad (15)$$

where $SFR(t)$ is the SFR for a GMC, $M_*(t)$ is the stellar mass associated with the GMC, and α_{fb} is the feedback parameter. SFR is further expressed as

$$SFR(t) = -SFE_{\text{ff},i} \frac{M_{\text{GMC}}(t)}{\tau_{\text{ff}}}, \quad (16)$$

where SFE_{ff,i} is the *intrinsic* star formation efficiency per free-fall time. We use the notation SFE_{ff,i} to distinguish it from the observationally derived, SFE_{ff}. The stellar mass is obtained simply by integrating $SFR(t)$:

$$M_*(t) = \int_0^t |SFR(t')| dt'. \quad (17)$$

Solving these equations, M_{GMC} and M_* are described as a function of time.

The observationally derived SFR just traces the stellar mass that is formed within a fixed time window. Denoting the observed apparent value of the SFR as SFR_a, it can be derived as

$$SFR_a(t) = \frac{\int_{\max(t-t_{\text{avg}}, 0)}^t M_*(t') dt'}{t_{\text{avg}}}, \quad (18)$$

where t_{avg} is the time window traced by the SFR tracer. As we use the H α emission as a tracer of the SFR, we fix t_{avg} as 4 Myr. If a cloud is younger than t_{avg} , then SFR_a for the cloud underestimates the actual SFR because of the fixed averaging window used in the denominator. Using the computed SFR_a(t), SFE_{ff} for a model cloud can be described as

$$SFE_{\text{ff}}(t) = \frac{SFR_a(t)}{M_{\text{GMC}}(t)} \tau_{\text{ff}}. \quad (19)$$

We adopt $\tau_{\text{ff}} = 6.7$ Myr and SFE_{ff,i} = 0.01 as representative values for the GMCs in M83. Although the actual value of α_{fb} is not unknown, we can derive it by assuming the lifetime of GMC because with the preceding equation, the lifetime of a model cloud is given as $\sim 0.5\pi / \sqrt{\alpha_{\text{fb}} SFE_{\text{ff},i} / \tau_{\text{ff}}}$ (Feldmann & Gnedin 2011). The estimated value of the GMC lifetime varies between 15 to 40 Myr (e.g., Kawamura et al. 2009; Murray 2011; Miura et al. 2012). To check the maximum influence the feedback can exert, we here adopt the smallest value of 15 Myr: α_{fb} is derived as 7.3 Myr^{-1} .

Figure 17 plots the observed SFE_{ff} as a function of the cloud mass for each region (a–h). In addition, figure 17(i) shows the evolutionary tracks for model clouds with initial masses of 10^6 and $10^7 M_{\odot}$, respectively. Along each of the two tracks, the squares indicate the time steps for 10%, 30%, 50%, 70%, and 90% of the lifetime of the model GMC, from the bottom to the top.

Initially, the model clouds move up almost straight on the plot as SFE_{ff} increases, which is driven by the rapid growth of the observed SFR. This rapid growth of the observed SFR is due to the underestimation of the observed SFR when the cloud's age is lower than t_{avg} , as stated above. Even after the initial rapid growth of SFE_{ff}, it continues to rise because the decrease in the cloud mass is always faster than the SFR decreases due to the averaging time imposed in the derivation of the SFR.

With the adopted parameters, the range of the values for SFE_{ff} is predicted to be within approximately 0.0038–0.024 for the 80% of the GMC lifetime, which is approximately equivalent to a ± 0.4 dex variation. The calculated range is indicated as the shaded area in figure 17 to aid comparison with the actual SFE_{ff} of the GMCs in M83. We note that this range is obtained by adopting the shortest estimate of the GMC lifetime available. If a longer GMC lifetime is assumed, then the range covered by SFE_{ff} becomes narrower. For example, if the assumed lifetime is 30 Myr, the variation is approximately ± 0.2 dex.

6.1.3.2 Comparison with the observed distribution of SFE_{ff} .

Up to now, we have seen that the evolutionary effect of a cloud might cause a variation in the apparent efficiency, SFE_{ff} , even if the intrinsic efficiency is fixed as $SFE_{\text{ff},i} = 0.01$. The predicted amount of the variation in SFE_{ff} is up to approximately ± 0.4 dex over 80% of the cloud lifetime, assuming the most intense role of the stellar feedback. Therefore, if the observed variation in SFE_{ff} is over the predicted range of SFE_{ff} obtained by assuming a fixed value of $SFE_{\text{ff},i}$, then $SFE_{\text{ff},i}$ is suggested to be nonuniform.

Comparing the observed SFE_{ff} of GMCs with the predicted range of SFE_{ff} in figure 17, we see that many GMCs deviate from the predicted ± 0.4 dex range of variations and also see signs of regional variations in the efficiency of star formation. For example, in the inter-arm regions, most of the GMCs, especially GMCs more massive than $10^6 M_{\odot}$ are located below the lower end of the predicted range that corresponds to the 10% of the model GMC lifetime. Thus, if $SFE_{\text{ff},i}$ is to be fixed as 0.01, then most of the GMCs in the inter-arm regions have to be in the very young stage of cloud evolution, younger than 10% of the assumed cloud lifetime. However, this appears implausible, because the dwelling time in the inter-arm regions observed here should be several tens of Myr, taking into consideration galactic dynamics (see figure 17 in Hirota et al. 2014). Therefore, the intrinsic efficiency, $SFE_{\text{ff},i}$, should be significantly lower than the global average of 0.01 in the inter-arm regions.

Another sign of regional variation in SFE_{ff} can be seen in the primary arm ridge, where a non-negligible number of GMCs exhibit an SFE_{ff} higher than the predicted range for it. Applying the argument same as for the inter-arm regions, the upward deviation of the observed SFE_{ff} in the primary arm ridge suggests that GMCs form stars with an $SFE_{\text{ff},i}$ that is higher than 0.01.

Here, we have seen that the range of observed variation in SFE_{ff} is larger than its allowed range of variation with a fixed value of $SFE_{\text{ff},i}$. We also have seen regional variations in the distributions of SFE_{ff} which suggests variation in $SFE_{\text{ff},i}$. Therefore, we conclude that the observed variation in SFE_{ff} is not just an artifact caused by the rapid mass consumption of GMCs due to the stellar feedback.

6.2 Impact of stellar feedback in limiting the lifetime of GMCs

As we have seen in §4.7, the GMC mass function in the primary arm exhibited a steeper slope (~ -1.8) compared to those in the other regions. Disruption of GMCs due to the role of stellar feedback was argued as a possible mechanism for the steeper slope of the GMC function in the primary arm ridge. To check the validity of the argument made in §4.7, we examine the impact of stellar feedback in this subsection.

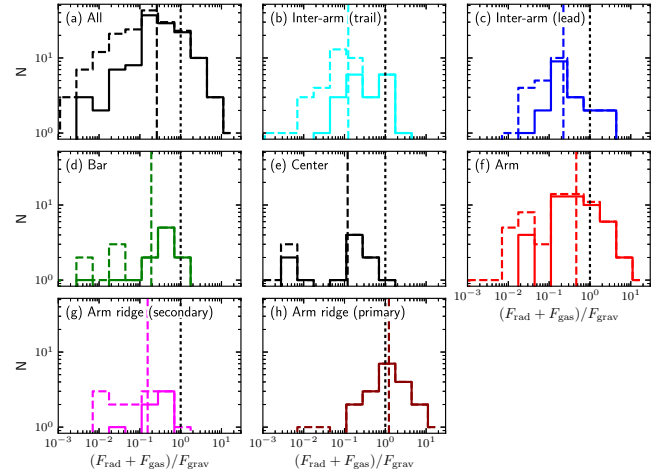


Fig. 18. Histogram of the ratio of the outward force, which is a combination of radiation and gas pressure forces, to the self-gravity of GMC, $(F_{\text{rad}} + F_{\text{gas}})/F_{\text{grav}}$, for each region. In each plot, the solid histogram shows the number distribution of the GMCs that have associated H II regions. The dashed histogram in each plot includes both GMCs with and without associated H II regions. Dotted and dashed vertical lines in each plot indicate $(F_{\text{rad}} + F_{\text{gas}})/F_{\text{grav}} = 1$ and median value of $(F_{\text{rad}} + F_{\text{gas}})/F_{\text{grav}}$ for the samples.

Stellar feedback takes place in various forms, such as momentum input by radiation pressure, gas pressure, stellar winds, and photo-ionization and photo-dissociation due to UV and FUV radiation. At the scale of 10–100 pc which is relevant to GMCs, the radiation pressure and gas pressure associated with warm ionized gas are considered to play dominant roles in removing gas material from host GMC (e.g., Matzner 2002; Lopez et al. 2011; Murray 2011). Here, we compare the outward force exerted by radiation pressure (F_{rad}) and ionized gas pressure (F_{gas}) against the inward force of gravity for each GMC to see if stellar feedback is indeed strong enough to destroy the GMCs in M83.

The force due to the radiation pressure from an H II region is calculated as

$$F_{\text{rad}} = L_{\text{bol}}/c, \quad (20)$$

where L_{bol} is the bolometric luminosity of an H II region and c is the speed of light. The derivation of L_{bol} for a GMC is made by converting back the SFR of the GMC (derived in §5.2) into the extinction-corrected H α luminosity using equation (13), and then applying a bolometric-to-H α luminosity ratio is calculated using Starburst99. The parameters used for the calculation are taken to be as same as those used in Calzetti et al. (2007) to maintain consistency with the SFR calibration described in §5.1.2. We must note that the equation only considers the direct radiation emitted by massive stars. In reality, emission absorbed by dust and re-emitted in infrared would boost

the radiation pressure. We omit this dust-processed emission from the calculation of radiation pressure for the following two reasons. First, the dust-processed emission is not the most dominant source of the pressure for normal HII regions in a galactic disk (Lopez et al. 2011; Lopez et al. 2014). Second, the calculation of the dust-processed emission requires computations of dust opacity that are far from trivial. As the dust-processed radiation should have a non-negligible impact in the central region, it should be noted that the outward pressure estimated in this subsection is likely to be an underestimate for the central region.

The force due to the pressure associated with warm ionized gas around an HII region is calculated as

$$F_{\text{gas}} = 4\pi R_{\text{HII}}^2 (2n_e k T_{\text{HII}}), \quad (21)$$

where R_{HII} is the radius of the HII region, n_e is the electron number density, k is the Boltzmann constant, and T_{HII} is the ionized gas temperature. We assume constant temperature of $T_{\text{HII}} = 10^4$ K. The number density of electrons is estimated as $n_e = \sqrt{3Q_{\text{Ly}\alpha}/(4\pi R_{\text{HII}}^3 \alpha_{\text{rec}})}$, where $Q_{\text{Ly}\alpha}$ is the Lyman continuum production rate and α_{rec} is the recombination coefficient. By assuming Case B recombination, $Q_{\text{Ly}\alpha}$ is derived from the H α luminosity for each HII region.

The force of gravity for a GMC is calculated as

$$F_{\text{grav}} = G \frac{M_{\text{GMC}}^2}{R^2}. \quad (22)$$

Figure 18 shows the distribution of the ratio of the outward force to the inward force, which is $(F_{\text{rad}} + F_{\text{gas}})/F_{\text{grav}}$. The radiation and gas pressure, F_{rad} and F_{gas} , calculated for each HII region is divided among the associated GMCs using the same method adopted for the SFR (§5.2). The median value of $(F_{\text{rad}} + F_{\text{gas}})/F_{\text{grav}}$ in the primary arm ridge is close to or above unity, suggesting that many GMCs in this region are certainly being disrupted by stellar feedback. On the other hand, $(F_{\text{rad}} + F_{\text{gas}})/F_{\text{grav}}$ is mostly below 1 in other regions. We again note that for the central region, $(F_{\text{rad}} + F_{\text{gas}})/F_{\text{grav}}$ is highly uncertain due to the omission of dust-processed radiation, and thus we do not discuss the central region here. As far as subregions in the disk of M83 are concerned, stellar feedback is most efficiently disrupting GMCs in the primary arm. This effectiveness of stellar feedback in the primary arm ridge is in agreement with the expectation that stellar feedback is responsible for forming the steeper slope of the mass function in this region.

As a by-product of the analysis made here, an approximate estimate of the lifetime of the GMCs can be made. First, we assume that GMCs evolve from a quiescent state in which they form a small amount of stars—and thus $(F_{\text{rad}} + F_{\text{gas}})/F_{\text{grav}} < 1$ —to an active state in which they form many massive stars—and thus $(F_{\text{rad}} + F_{\text{gas}})/F_{\text{grav}} > 1$. For the active GMCs with $(F_{\text{rad}} + F_{\text{gas}})/F_{\text{grav}} > 1$, it would be natural to assume further

that they are about to be disrupted by the stellar feedback and thus the average remaining lifetime for them is comparable to the nominal lifetime of massive stars. If stellar feedback is the only process that limits the lifetime of GMCs, then it is possible to gauge their lifetime from the number ratio of GMCs with $(F_{\text{rad}} + F_{\text{gas}})/F_{\text{grav}}$ above and below 1. Applying a similar method, the lifetime of a GMC is estimated to be 15–40 Myr in the MW (Williams & McKee 1997; Murray 2011), Large Magellanic Clouds (Kawamura et al. 2009) and M33 (Miura et al. 2012). For the GMCs in M83, 37 out of 179 are found to have $(F_{\text{rad}} + F_{\text{gas}})/F_{\text{grav}}$ greater than 1. Taking that average lifetime of massive stars as 4 Myr, the average lifetime of a GMC is estimated to be ~ 20 Myr ($= 179/37 \times 4$ Myr), which is not far from the estimation made for other galaxies. However, this estimation has to be treated with great care because it is merely an averaged value found in the limited area presented here, and it also does not take into consideration the role of shear that might be responsible for disrupting GMCs in the inter-arm regions (Meidt et al. 2015).

6.3 Implications of the spatial variation in SFE

The cloud-scale examination of SFE_{ff} made in §5.5 indicated the following three points: (1) mass-weighted mean value of SFE_{ff} is $\sim 0.93\%$, which is in agreement with the average values found in other systems (e.g., Krumholz et al. 2012); (2) however there is a large scatter in SFE_{ff} with a MAD of ~ 0.6 dex and peak-to-peak variation of approximately three orders of magnitude; and (3) there is a regional variation in SFE_{ff} . The most prominent characteristic of the regional variation in SFE_{ff} is the high median SFE_{ff} in the primary arm ridge (~ 0.027), compared to the inter-arm regions (4.6×10^{-3} and 2.7×10^{-3}) and the secondary arm ridge ($\sim 3.9 \times 10^{-3}$). In this subsection, we discuss the implications of these findings.

There is a group of theories that focus on the roles of turbulence in regulating star formation, and aim to provide a quantitative description which produces $\text{SFE}_{\text{ff}} \simeq 0.01$ in a steady state (e.g., Krumholz & McKee 2005; Federrath 2015). The goal of achieving $\text{SFE}_{\text{ff}} \simeq 0.01$ in a steady state implies that GMCs are approximated as long-lived entities that form stars with a stable efficiency. The first point, the mass-weighted mean of SFE_{ff} being approximated 0.01, agree with the expectation of the turbulence-regulated model. However, the second point, the large scatter in the apparent distribution of SFE_{ff} does not agree with the assumption of stable efficiency in GMCs.

Although the turbulence-regulated model of star formation is well applied to some studies made with mostly coarse resolutions that sample several clouds per beam (e.g., Krumholz et al. 2012), it has been argued that the cloud-scale distribution of SFE_{ff} show some deviations from the expectation of turbulence-regulated models (Murray 2011; Lee et al. 2016). In

particular, Lee et al. (2016) observed a large scatter in SFE_{ff} in Galactic GMCs, and they argued that it is difficult to explain the large scatter in SFE_{ff} with the models of turbulence-regulated star formation, including Krumholz & McKee (2005), Padoan & Nordlund (2011) and Hennebelle & Chabrier (2011). Instead, they claimed that SFE_{ff} should be a time-dependent variable that dynamically increases during the lifetime of GMCs; at the later phase of their lifetime, GMCs produce stars with high SFE_{ff} and are disrupted by stellar feedback.

The spread in SFE_{ff} observed in M83 is similarly huge as the one observed in Galactic GMCs by Lee et al. (2016), and therefore the idea that SFE_{ff} increases with time might also hold in M83. The SFE_{ff} observed in Galactic GMCs by Lee et al. (2016) is characterized by a median and scatter about the median of $\sim 1.8\%$ and 0.91 dex, respectively. The scatter of 0.91 dex is comparable with the MAD of ~ 0.6 dex observed in M83.² We note that the median SFE_{ff} of $\sim 1.8\%$ obtained by Lee et al. (2016) is higher than the one obtained here in M83 (0.3%), but it is likely due to the fact that Lee et al. (2016) has selected GMCs with active star formation. It is also noteworthy that Leroy et al. (2017) also found the median value of SFE_{ff} in M51 to be $\sim 0.3\%$ with a resolution of 370 pc.

If the notion that SFE_{ff} increases with time during the lifetime of a GMC is correct, then the regional variations of SFE_{ff} (the third point) may suggest that large-scale galactic structures exert an influence in organizing the life cycle of GMCs. The GMCs in the primary arm ridge exhibit a higher SFE_{ff} compared to the inter-arm GMCs. If SFE_{ff} increases over the lifetimes of GMCs, the GMCs in the primary arm ridge should be at a late stage of their evolution, producing stars with increased SFE_{ff} , while GMCs in the inter-arm regions are at an early stage with low SFE_{ff} . The idea that GMCs in the primary arm ridge are at a late stage of their evolution is in agreement with the analysis made in §6.2, which suggested that the GMCs in the primary arm ridge are about to be disrupted by stellar feedback (§6.2).

The discussion so far can be summarized as follows: SFE_{ff} increases with time during the lifetime of a GMC and galactic structures have a certain role in organizing the lifetimes of GMCs. This scenario is in agreement with the suggestion that spiral arms can organize the buildup of massive GMCs (Egusa et al. 2011; Colombo et al. 2014). A concern is the timescale of traversal across inter-arm regions which can be a factor of few longer than the suggested lifetime of GMCs, which is 15–40 Myr. If all GMCs have the same lifetime and also increased SFE_{ff} in the same way, then at least a few GMCs in the inter-arm should exhibit SFE_{ff} values as high as those in the primary arm ridge. However, the inter-arm GMCs do not exhibit such a high SFE_{ff} . Therefore, to explain the observed SFE_{ff} ,

a mechanism that obstructs the evolution of GMCs in the inter-arm regions would be required. The large-scale shear that acts to disrupt clouds (Meidt et al. 2015) might be a candidate mechanism. If there exists a mechanism that disrupts GMCs in the inter-arm before increasing SFE_{ff} , the lifetime of GMCs in the arm and inter-arm could be different from each other. Complete mapping of a galaxy in CO and reliable star formation tracers will be required to fully reveal the life cycle of GMCs.

7 Summary

Results of the mosaic ^{12}CO (1–0) observations of the nearby barred galaxy M83 carried out with ALMA are presented. The interferometric data are combined with the data obtained with the Nobeyama 45-m telescope to recover the total flux. The mosaic observations cover a ~ 13 kpc² region that includes the galactic center, eastern bar and spiral arm with a spatial resolution of $2''.03 \times 1''.15$ (44.3 pc \times 25.1 pc), which is comparable to the typical sizes of GMCs. The velocity resolution is ~ 2.5 km s⁻¹.

- With the GMC scale resolution, galactic structures including the spiral arm and the bar are resolved into narrow structures. The bar appears as a continuous molecular ridge with a surface density as high as 200–800 M_{\odot} pc⁻², which exceeds the surface density of typical Galactic GMCs. The spiral arm is resolved into two ridges, or chains of molecular clouds, that run parallel to each other. The one at the leading side, referred to as primary arm ridge, is associated with numerous bright H II regions while the other one at the trailing side, referred to as secondary arm ridge, appears to be more quiescent. Spurs are found at the leading side of the primary arm ridge and the bar.
- The distribution of the massive star-forming regions exhibits a higher degree of concentration, compared to that of CO emission. Most of the H II regions are concentrated in particular regions, including the primary arm ridge and the bar, which suggests a spatial variation in the SFE.
- We identify 179 GMCs from the CO data using the *astroden-dro* software package. When making the cloud identification, the data cube is smoothed in the spatial directions to a resolution of $2''.1$ (~ 46 pc). Assuming the Galactic CO-to-H₂ conversion factor, the median value of the cloud mass is found to be $1.6 \times 10^6 M_{\odot}$. The virial mass and CO luminosity are well correlated to each other, and the median value of the virial parameter for all the identified GMCs is found to be ~ 1.4 , suggesting that most of the GMCs are strongly influenced by their self-gravity. The GMCs in the arm exhibited lower virial parameters with the median value of ~ 1.0 .
- The mass spectrum for all the identified GMCs are fitted with a truncated power law with a slope of -1.58 ± 0.1 , which is close to that of the Galactic GMCs. The fitting is also per-

² If the distribution in figure 16(a) is approximated as a Gaussian, a MAD of 0.6 dex corresponds to a scatter of ~ 0.9 dex

formed for GMCs in each subregion, and the steepest slope is found in the primary arm ridge (-1.8). We suggest that GMCs in the primary arm ridge are disrupted due to stellar feedback.

- The identified GMCs are cross-matched with the catalog of H II regions to estimate the SFR for each GMC. As the star formation history for individual H II regions is not constrained, there should be a factor-of-2 uncertainty in the calibration of the SFR. Despite this weakness, the overall statistical distribution of the SFE for the GMCs in M83 are found to be in agreement with that of Galactic clouds. The median SFE is $\sim 0.5 \text{ Gyr}^{-1}$ and the scatter is as large with a peak to peak variation of approximately two orders of magnitude.
- The mass-weighted mean of SFE_{ff} is $\sim 9.4 \times 10^{-3}$, which is in agreement with the expectations of turbulence regulated star formation models. However, its scatter is as large as ~ 0.7 dex in MAD, which cannot be explained by a cloud evolution model with a constant SFE_{ff} . In addition, a regional variation in SFE_{ff} is also observed. The median value of SFE_{ff} is highest in the primary arm ridge (~ 0.027) while it is more than a factor of 5 lower in the inter-arm regions and in the secondary arm ridge. The large spread and significant spatial variation observed in SFE_{ff} support the idea that SFE_{ff} is not a steady time-invariant variable, but is a dynamic variable that increases as GMCs evolve. In particular, the GMCs in the primary arm ridges are suggested to be reaching the last stage of their evolution with elevated SFE_{ff} , because the feedback from massive stars appears to be large enough to disrupt them.

Acknowledgments

We would like to thank the referee for carefully reading the paper and proving valuable comments. This paper makes use of the following ALMA data: ADS/JAO.ALMA#2011.0.00772.S. ALMA is a partnership of ESO (representing its member states), NSF (USA), and NINS (Japan), together with NRC (Canada), NSC and ASIAA (Taiwan), and KASI (Republic of Korea), in cooperation with the Republic of Chile. The Joint ALMA Observatory is operated by ESO, AUI/NRAO, and NAOJ. This research made use of images provided by the Survey for Ionization in Neutral Gas Galaxies (Meurer et al. 2006) which is partially supported by the National Aeronautics and Space Administration (NASA). This research has made use of the NASA/IPAC Extragalactic Database (NED) which is operated by the Jet Propulsion Laboratory, California Institute of Technology, under contract with the National Aeronautics and Space Administration. This research made use of *astrodendro*, a Python package to compute dendrograms of Astronomical data (<http://www.dendrograms.org/>). This research made use of *APLpy*, an open-source plotting package for Python hosted

at <http://aplpy.github.com>.

References

- Ballesteros-Paredes, J., Hartmann, L. W., Vázquez-Semadeni, E., Heitsch, F., & Zamora-Avilés, M. A. 2011, *MNRAS*, 411, 65
- Bertoldi, F., & McKee, C. F. 1992, *ApJ*, 395, 140
- Blitz, L., & Shu, F. H. 1980, *ApJ*, 238, 148
- Bolatto, A. D., Wolfire, M., & Leroy, A. K. 2013, *ARA&A*, 51, 207
- Bresolin, F., Kudritzki, R.-P., Urbaneja, M. A., et al. 2016, *ApJ*, 830, 64
- Calzetti, D., et al. 2007, *ApJ*, 666, 870
- Calzetti, D., Chandar, R., Lee, J. C., et al. 2010, *ApJL*, 719, L158
- Cardelli, J. A., Clayton, G. C., & Mathis, J. S. 1989, *ApJ*, 345, 245
- Chomiuk, L., & Povich, M. S. 2011, *AJ*, 142, 197
- Colombo, D., Hughes, A., Schinnerer, E., et al. 2014, *ApJ*, 784, 3
- Comte, G. 1981, *A&AS*, 44, 441
- Crosthwaite, L. P., Turner, J. L., Buchholz, L., Ho, P. T. P., & Martin, R. N. 2002, *AJ*, 123, 1892
- de Vaucouleurs, G., de Vaucouleurs, A., Corwin, H. G., Jr., Buta, R. J., Paturel, G., & Fouque, P. 1991, Volume 1-3, XII, 2069 pp. 7 figs.. Springer-Verlag Berlin Heidelberg New York,
- Dobbs, C. L. 2008, *MNRAS*, 391, 844
- Dobbs, C. L., & Bonnell, I. A. 2006, *MNRAS*, 367, 873
- Dopita, M. A., & Sutherland, R. S. 2003, *Astrophysics of the diffuse universe*, Berlin, New York: Springer, 2003. Astronomy and astrophysics library, ISBN 3540433627
- Egusa, F., Koda, J., & Scoville, N. 2011, *ApJ*, 726, 85
- Elmegreen, D. M. 1980, *ApJ*, 242, 528
- Elmegreen, D. M., Chromey, F. R., & Warren, A. R. 1998, *AJ*, 116, 2834
- Evans, N. J., II, Dunham, M. M., Jørgensen, J. K., et al. 2009, *ApJS*, 181, 321-350
- Faesi, C. M., Lada, C. J., Forbrich, J., Menten, K. M., & Bouy, H. 2014, *ApJ*, 789, 81
- Federrath, C. 2015, *MNRAS*, 450, 4035
- Feldmann, R., & Gnedin, N. Y. 2011, *ApJL*, 727, L12
- Freeman, P., Rosolowsky, E., Kruijssen, J. M. D., Bastian, N., & Adamo, A. 2017, *MNRAS*, 468, 1769
- Fukui, Y., Kawamura, A., Minamidani, T., et al. 2008, *ApJS*, 178, 56-70
- Goldreich, P., & Kwan, J. 1974, *ApJ*, 189, 441
- Gratier, P., Braine, J., Rodriguez-Fernandez, N. J., et al. 2012, *A&A*, 542, A108
- Heald, G., de Blok, W. J. G., Lucero, D., et al. 2016, *MNRAS*, 462, 1238
- Hennebelle, P., & Chabrier, G. 2011, *ApJL*, 743, L29
- Heyer, M. H., Carpenter, J. M., & Snell, R. L. 2001, *ApJ*, 551, 852
- Heyer, M. H., & Brunt, C. M. 2004, *ApJL*, 615, L45
- Heyer, M., Krawczyk, C., Duval, J., & Jackson, J. M. 2009, *ApJ*, 699, 1092
- Heyer, M., & Dame, T. M. 2015, *ARA&A*, 53, 583
- Hirota, A., Kuno, N., Sato, N., et al. 2011, *ApJ*, 737, 40
- Hirota, A., Kuno, N., Baba, J., et al. 2014, *PASJ*, 66, 46
- Hughes, A., Meidt, S. E., Colombo, D., et al. 2013, *ApJ*, 779, 46
- Inutsuka, S.-i., Inoue, T., Iwasaki, K., & Hosokawa, T. 2015, *A&A*, 580, A49
- Jarrett, T. H., Masci, F., Tsai, C. W., et al. 2013, *AJ*, 145, 6
- Kawamura, A., Mizuno, Y., Minamidani, T., et al. 2009, *ApJS*, 184, 1
- Kennicutt, R. C., Jr. 1998, *ApJ*, 498, 541
- Kobayashi, M. I. N., Inutsuka, S.-i., Kobayashi, H., & Hasegawa, K. 2017,

- ApJ, 836, 175
- Koda, J., et al. 2009, ApJL, 700, L132
- Koda, J., Yagi, M., Boissier, S., et al. 2012, ApJ, 749, 20
- Koda, J., Scoville, N., & Heyer, M. 2016, ApJ, 823, 76
- Kroupa, P. 2001, MNRAS, 322, 231
- Krumholz, M. R., & McKee, C. F. 2005, ApJ, 630, 250
- Krumholz, M. R., Dekel, A., & McKee, C. F. 2012, ApJ, 745, 69
- Kuno, N., et al. 2007, PASJ, 59, 117
- Kurono, Y., Morita, K.-I., & Kamazaki, T. 2009, PASJ, 61, 873
- Lada, C. J., Lombardi, M., & Alves, J. F. 2010, ApJ, 724, 687
- Larsen, S. S., & Richtler, T. 1999, A&A, 345, 59
- Larson, R. B. 1981, MNRAS, 194, 809
- La Vigne, M. A., Vogel, S. N., & Ostriker, E. C. 2006, ApJ, 650, 818
- Lee, Y., Snell, R. L., & Dickman, R. L. 1994, ApJ, 432, 167
- Lee, Y., Snell, R. L., & Dickman, R. L. 1996, ApJ, 472, 275
- Lee, E. J., Miville-Deschênes, M.-A., & Murray, N. W. 2016, ApJ, 833, 229
- Leitherer, C., Schaerer, D., Goldader, J. D., et al. 1999, ApJS, 123, 3
- Leroy, A. K., Lee, C., Schrubba, A., et al. 2013, ApJL, 769, L12
- Leroy, A. K., Bolatto, A. D., Ostriker, E. C., et al. 2015, ApJ, 801, 25
- Leroy, A. K., Schinnerer, E., Hughes, A., et al. 2017, ApJ, 846, 71
- Lopez, L. A., Krumholz, M. R., Bolatto, A. D., Prochaska, J. X., & Ramirez-Ruiz, E. 2011, ApJ, 731, 91
- Lopez, L. A., Krumholz, M. R., Bolatto, A. D., et al. 2014, ApJ, 795, 121
- Imara, N. 2015, ApJ, 803, 38
- Mac Low, M.-M., & Klessen, R. S. 2004, Reviews of Modern Physics, 76, 125
- Maddalena, R. J., & Thaddeus, P. 1985, ApJ, 294, 231
- Matzner, C. D. 2002, ApJ, 566, 302
- McMullin, J. P., Waters, B., Schiebel, D., Young, W., & Golap, K. 2007, Astronomical Data Analysis Software and Systems XVI, 376, 127
- Megeath, S. T., Allgaier, E., Young, E., et al. 2009, AJ, 137, 4072
- Meidt, S. E., Hughes, A., Dobbs, C. L., et al. 2015, ApJ, 806, 72
- Meurer, G. R., Hanish, D. J., Ferguson, H. C., et al. 2006, ApJS, 165, 307
- Miura, R. E., Kohno, K., Tosaki, T., et al. 2012, ApJ, 761, 37
- Mooney, T. J., & Solomon, P. M. 1988, ApJL, 334, L51
- Murray, N. 2011, ApJ, 729, 133
- Orear, J. 1982, American Journal of Physics, 50, 912
- Padoan, P., & Nordlund, Å. 2011, ApJ, 730, 40
- Petry, D., & CASA Development Team 2012, Astronomical Data Analysis Software and Systems XXI, 461, 849
- Rand, R. J., Kulkarni, S. R., & Rice, W. 1992, ApJ, 390, 66
- Rand, R. J., Lord, S. D., & Higdon, J. L. 1999, ApJ, 513, 720
- Renaud, F., Bournaud, F., Emsellem, E., et al. 2013, MNRAS, 436, 1836
- Rosolowsky, E. 2005, PASP, 117, 1403
- Rosolowsky, E., & Leroy, A. 2006, PASP, 118, 590
- Rosolowsky, E., Keto, E., Matsushita, S., & Willner, S. P. 2007, ApJ, 661, 830
- Sakamoto, K., Matsushita, S., Peck, A. B., Wiedner, M. C., & Iono, D. 2004, ApJL, 616, L59
- Sanders, D. B., Scoville, N. Z., & Solomon, P. M. 1985, ApJ, 289, 373
- Sault, R. J., Teuben, P. J., & Wright, M. C. H. 1995, in ASP Conf. Ser. 77, Astronomical Data Analysis Software and Systems IV, ed. R. A. Shaw, H. E. Payne, & J. J. E. Hayes (San Francisco, CA: ASP), 433
- Sawada, T., et al. 2008, PASJ, 60, 445
- Schinnerer, E., Meidt, S. E., Colombo, D., et al. 2017, ApJ, 836, 62
- Schlegel, D. J., Finkbeiner, D. P., & Davis, M. 1998, ApJ, 500, 525
- Scoville, N. Z., Polletta, M., Ewald, S., et al. 2001, AJ, 122, 3017
- Sheth, K., Regan, M. W., Vogel, S. N., & Teuben, P. J. 2000, ApJ, 532, 221
- Solomon, P. M., Rivolo, A. R., Barrett, J., & Yahil, A. 1987, ApJ, 319, 730
- Thatte, N., Tecza, M., & Genzel, R. 2000, A&A, 364, L47
- Thilker, D. A., Braun, R., & Walterbos, R. A. M. 2000, AJ, 120, 3070
- Thim, F., Tammann, G. A., Saha, A., Dolphin, A., Sandage, A., Tolstoy, E., & Labhardt, L. 2003, ApJ, 590, 256
- Tilanus, R. P. J., & Allen, R. J. 1993, A&A, 274, 707
- Tosaki, T., Kohno, K., Harada, N., et al. 2017, PASJ, 59, 117
- Utomo, D., Blitz, L., Davis, T., et al. 2015, ApJ, 803, 16
- Venuti, L., Prisinzano, L., Sacco, G. G., et al. 2018, A&A, 609, A10
- Wada, K., & Koda, J. 2004, MNRAS, 349, 270
- Walter, F., Brinks, E., de Blok, W. J. G., et al. 2008, AJ, 136, 2563
- Whitworth, A. 1979, MNRAS, 186, 59
- Wiklund, T., Rydbeck, G., Hjalmarsen, A., & Bergman, P. 1990, A&A, 232, L11
- Wilson, C. D., & Scoville, N. 1990, ApJ, 363, 435
- Williams, J. P., & McKee, C. F. 1997, ApJ, 476, 166
- Wong, T., Hughes, A., Ott, J., et al. 2011, ApJS, 197, 16
- Zuckerman, B., & Evans, N. J., II 1974, ApJL, 192, L149
- Zurita, A., & Pérez, I. 2008, A&A, 485, 5